

# **Early warning for great earthquakes from characterization of crustal deformation patterns with deep learning**

**J-T. Lin<sup>1</sup>, D. Melgar<sup>1</sup>, A. M. Thomas<sup>1</sup>, and J. Searcy<sup>2</sup>**

<sup>1</sup>Department of Earth Sciences, University of Oregon, Eugene, Oregon, USA

<sup>2</sup>Research Advanced Computing Services, University of Oregon, Eugene, Oregon, USA

Corresponding author: Jiun-Ting Lin ([jiunting@uoregon.edu](mailto:jiunting@uoregon.edu))

This is a non-peer reviewed preprint submitted to EarthArXiv. This paper has been submitted to the Journal of Geophysical Research – Solid Earth for review.

1 **Early warning for great earthquakes from characterization of crustal**  
2 **deformation patterns with deep learning**

3 **J-T. Lin<sup>1</sup>, D. Melgar<sup>1</sup>, A. M. Thomas<sup>1</sup>, and J. Searcy<sup>2</sup>**

4 <sup>1</sup>Department of Earth Sciences, University of Oregon, Eugene, Oregon, USA

5 <sup>2</sup>Research Advanced Computing Services, University of Oregon, Eugene, Oregon, USA

6 Corresponding author: Jiun-Ting Lin (jiunting@uoregon.edu)

7  
8  
9 **Abstract**

10 Although infrequent, large earthquakes (Mw8+) can be extremely damaging and occur on  
11 subduction and intraplate faults worldwide. Earthquake early warning (EEW) systems aim to  
12 provide advanced warning before strong shaking and tsunami onsets. These models estimate  
13 earthquake magnitude by the early metrics of waveforms, relying on empirical scaling  
14 relationships of abundant past events. However, both the rarity and complexity of great events  
15 make it challenging to characterize them, and EEW algorithms often underpredict magnitude and  
16 the resulting hazards. Here we propose a model, M-LARGE, that leverages the power of deep  
17 learning to characterize crustal deformation patterns of large earthquakes in real time. We  
18 generate realistic rupture scenarios and use these to train a model that directly measures  
19 earthquake magnitude from ground displacements. M-LARGE successfully performs reliable  
20 magnitude estimation on the testing dataset with an accuracy of 99% for simulated events and  
21 for five damaging historical earthquakes in the Chilean Subduction Zone. Unlike existing models  
22 which focus on the final earthquake magnitude, M-LARGE tracks the evolution of the source  
23 process and can make faster and more accurate magnitude estimates, frequently before rupture  
24 is complete. M-LARGE significantly outperforms currently operating EEW algorithms.

25

## 26 **1 Introduction**

27 Following earthquake initiation, most EEW algorithms provide the initial hazard predictions  
28 based on the character of the first arriving P-waves, which is the earliest information available.  
29 However, it is well known that this approach will routinely struggle during large magnitude  
30 earthquakes owing to magnitude saturation, or underestimation, a current limitation of such EEW  
31 systems. Saturation occurs for two reasons. First, inertial-based instruments (seismometers) that  
32 record earthquakes in the near-field tend to distort large, low-frequency, typically over tens to  
33 hundreds of seconds, signals radiated from large earthquakes, making the data unreliable ([Boore](#)  
34 [& Bommer, 2005](#); [Larson, 2009](#); [Bock & Melgar, 2016](#)). Second, large earthquakes have  
35 durations of several minutes and early onset signals (i.e. the first few seconds) might not contain  
36 enough information to forecast the final earthquake magnitude ([Rydelek & Horiuchi, 2006](#); [Meier](#)  
37 [et al., 2016, 2017](#); [Melgar & Hayes, 2017](#); [Ide, 2019](#); [Goldberg et al., 2019](#)). As an example of  
38 this, the Japanese EEW system mis-identified the 2011 Mw9.0 Tohoku-oki earthquake as only an  
39 Mw8.1 for the first hour after rupture ([Hoshiba et al., 2011](#)). This magnitude saturation has  
40 consequences for downstream applications that rely on rapid magnitude determination,  
41 specifically, in the 2011 Tohoku-oki case both forecasts of the expected shaking and the tsunami  
42 amplitudes were drastically underpredicted ([Colombelli et al., 2013](#); [Hoshiba et al., 2014](#)).

43

44 In recent years, a number of EEW algorithms that attempt to ameliorate the magnitude  
45 saturation problem have been developed and tested. For example it is possible to match shaking  
46 patterns in real-time to the expected geometric extension of the causative fault ([Böse et al., 2012](#);  
47 [Hutchison et al., 2020](#)). Another approach is to forego complete characterization of the  
48 earthquake, and simply take the observed shaking wavefield at a particular instant in time, and  
49 forecast its time-evolution into the future ([Kodera et al., 2018](#); [Cochran et al., 2019](#)). Furthermore,  
50 the advent of widespread high rate global navigation satellite system (HR-GNSS) networks have

51 enabled a new class of EEW algorithms based on measurements of crustal deformation and are  
52 particularly well suited to identifying large magnitude earthquakes (Crowell et al., 2013;  
53 Grapenthin et al., 2014; Minson et al., 2014; Kawamoto et al., 2016). Noteworthy among these  
54 are methods is the Geodetic First Approximation of Size and Time (GFAST) algorithm which is  
55 primarily based on the scaling of peak ground displacement (PGD) and is currently operating in  
56 U.S. EEW system for large earthquakes (Crowell et al., 2013, 2016).

57

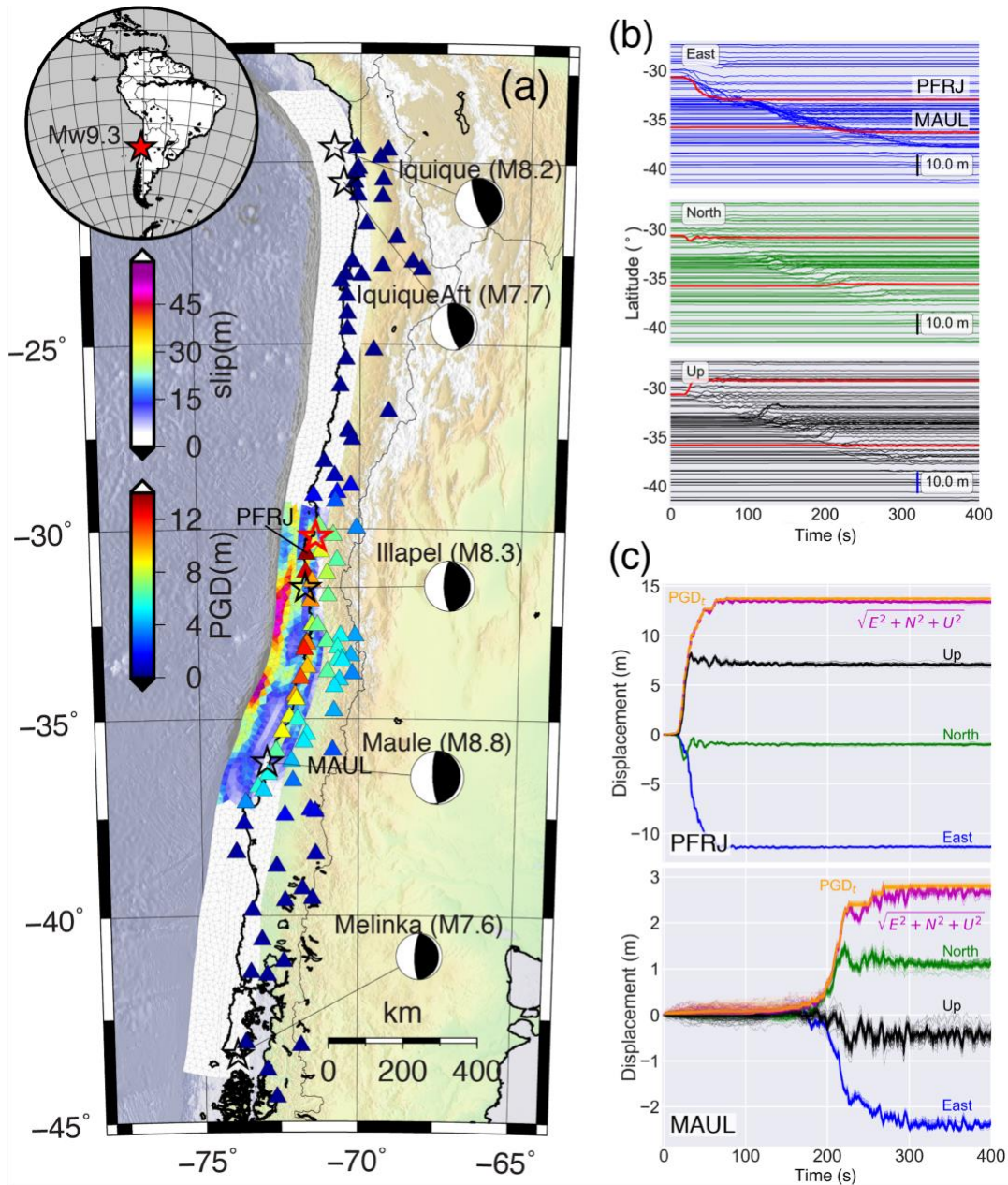
58 Despite the sophistication of these existing algorithms, many of which are employed in some  
59 of the most advanced EEW systems world wide (such as the U.S. and Japan) (Murray et al.,  
60 2018; Kodera et al., 2020), each of them has limitations. For example, the seismic wavefield-  
61 based approaches overcome saturation at the expense of short warning times, typically of the  
62 order of ~10-20s (Kodera et al., 2018). Meanwhile, PGD-based approaches avoid saturation but  
63 can struggle when earthquakes have very long or unilateral ruptures (Williamson et al., 2020) and  
64 can grossly over-predict the magnitudes of these kinds of events. At the root of these difficulties  
65 is that every large earthquake is different from the next. Each can, and likely will, have a different  
66 starting location, rupture velocity, slip distribution, and radiated seismic energy that evolves in a  
67 complex way as the rupture unfolds. All of these properties fundamentally affect EEW system  
68 performance and are difficult if not impossible to predict prior to earthquake occurrence. As such,  
69 developing algorithms that can reliably characterize this complexity from surface observations in  
70 real-time has proven challenging.

71

72 In spite of this diversity of earthquake characteristics, advances in seismic and geodetic  
73 instrumentation over the last 30 years have allowed observation and synthesis of the basic  
74 kinematic behaviors of large ruptures (Vallée & Douet, 2016; Ye et al., 2016; Hayes, 2017).  
75 Additionally, the location and geometry of the faults on which many large earthquakes are  
76 expected to occur are well known (Hayes et al., 2018). By combining these observations it is now

77 possible to efficiently simulate the rupture process of many potential earthquakes in a realistic  
78 way, and to predict their expected seismic and geodetic signatures ([Melgar et al., 2016](#); [Frankel  
79 et al., 2018](#); [Goldberg & Melgar, 2020](#); [Pitarka et al., 2020](#)).

80 Another important improvement, specifically in the case of HR-GNSS, is that noise models  
81 for real-time data have been proposed ([Geng et al., 2018](#); [Melgar et al., 2020](#)). HR-GNSS  
82 displacements are a derived product and there can be significant differences between real-time  
83 and post-processed solutions. This improvement enables adding realistic noise to any simulated  
84 waveform. In aggregate, this ability to efficiently simulate data from large earthquakes enables  
85 the use of deep learning algorithms ([LeCun et al., 2015](#)) that have been demonstrated to provide  
86 significant improvements in other data-rich seismological applications such as earthquake  
87 detection, phase picking, and association ([Perol et al., 2018](#); [Ross et al., 2018](#); [Kong et al., 2019](#);  
88 [Zhu & Beroza, 2019](#); [Mousavi et al., 2020a, 2020b](#)). Here, we will show how to leverage the  
89 powerful ability of deep-learning together with the aforementioned realistic earthquake  
90 simulations and their associated HR-GNSS waveforms to characterize earthquake magnitude in  
91 real-time. As a demonstration, we apply this approach to the Chilean Subduction Zone which has  
92 a dense real-time GNSS network and assess its performance on five recent large-magnitude  
93 earthquakes that have occurred there ([Figure 1](#)).



94

95 **Figure 1.** Map of the Chilean subduction zone, example rupture scenario, and resulting HR-GNSS

96 waveforms. (a) Slip distribution of a Mw9.3 earthquake. GNSS stations (triangles) colored by their PGD.

97 Focal mechanisms of 5 large events that have occurred since 2010. Red and black stars represent the

98 hypocenter of the Mw9.3 rupture scenario and of the historical earthquakes, respectively. (b) Three-

99 component GNSS time series sorted by latitude. Bold red lines denote the records at station PFRJ and

100 MAUL. (c) close-up of time series at stations PFRJ and MAUL. Thin lines denote the GNSS noise

101 introduced in the Data and Method section (see section 2.1).

102

## 103 **2 Data and Methods**

### 104 **2.1 M-LARGE : Model architecture and training**

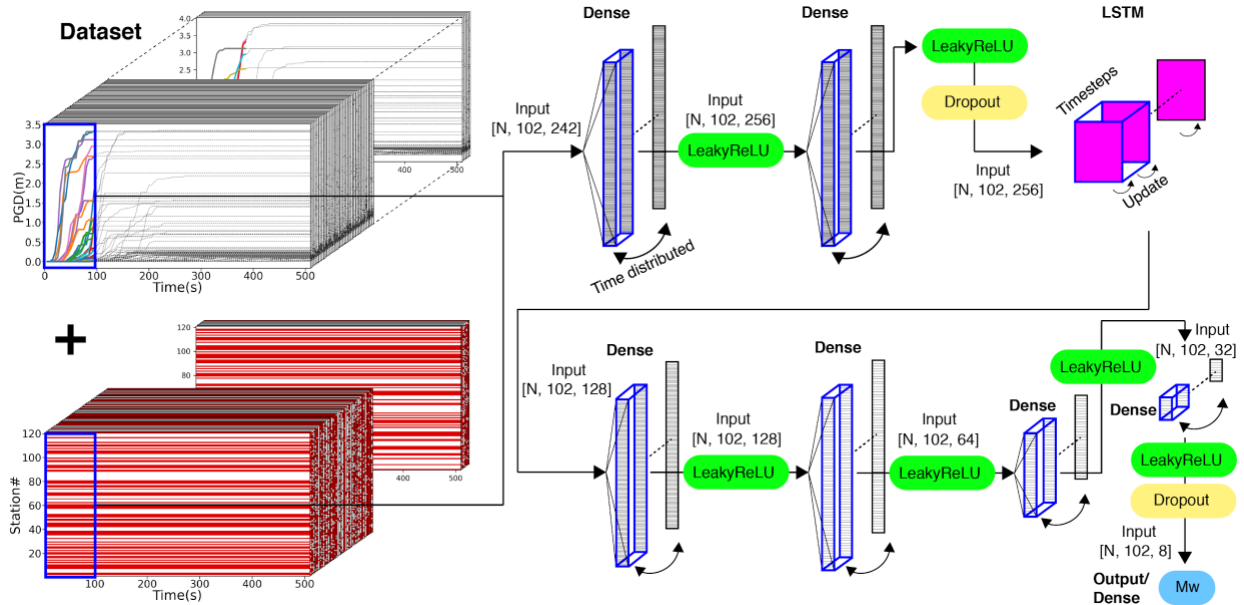
105 For time-dependent earthquake magnitude prediction we employ a deep-learning model, called  
106 Machine Learning Assessed Rapid Geodetic Earthquake magnitude (M-LARGE). It is composed  
107 of seven fully connected layers and a unidirectional long-short term memory (LSTM) recurrent  
108 layer (Hochreiter & Schmidhuber, 1997), which iteratively predicts  $M_w$  using the current and  
109 previous HR-GNSS observations across the network (Figure 2; Table 1; see section 2.4 for  
110 details). We adopted this model architecture because it is flexible enough to capture the  
111 complexities of large earthquakes, allows M-LARGE to update magnitude predictions as the  
112 rupture progresses, and it does not require *a-priori* source information (such as the hypocenter)  
113 typically required by other rapid modeling methods (e.g. Crowell et al., 2018).

114 M-LARGE is composed of seven dense (fully connected) layers wrapping an LSTM layer.  
115 Note that the dense layers only connect the feature values at the same time channel, rather than  
116 all the features, which would include future times as well. Dropouts are applied to prevent  
117 overfitting during the training process (Srivastava et al., 2014). We use a Leaky ReLU function  
118 with a slope of 0.1 at negative values (Mass et al., 2013), an adaptation of the regular ReLU  
119 (Glorot et al., 2011) for the activation for dense layers. Finally, the last layer is connected to a  
120 ReLU function to output a current magnitude prediction, and the goal is to minimize the mean  
121 square error (MSE) contributed from the magnitude misfits at every epoch (Figure 2). We  
122 generated 27,200 ruptures (the process is described in the next section) and split them into  
123 training (70%), validation (20%) and testing data (10%) (Figure S1, S2). We apply data  
124 augmentation by introducing realistic HR-GNSS noise and station incompleteness yielding more  
125 than 6 million earthquake and station scenarios used for 50,000 training steps (Figure S3). Details  
126 of the HR-GNSS noise and station incompleteness are provided in section 2.2 and section 2.3,  
127 respectively. We save the training weights every 5 epochs and use the model which has the

128 minimum validation loss as the best model. The code base is publically available and can be  
 129 obtained at <https://zenodo.org/record/4527253> (Lin, 2021).

130

131



132

133 **Figure 2.** M-LARGE model architecture showing the input as the time-dependent PGD values from the  
 134 GNSS stations plus the station on or off (existence) codes. Detailed parameter values are listed in [Table 1](#).

135 Blue rectangles mark the input PGD time series (i.e. 100 s) from all the available stations with their existence  
 136 codes, and the participating layers.

137

138 **Table 1.** List of parameter values used

Layer#	Name	Neurons/parameters	Input dimension	Output dimension
Layer0	Input	0	[N, 102, 242]	[N, 102, 242]
Layer1	Dense	256	[N, 102, 242]	[N, 102, 256]
Activation	LeakyReLU	0.1	[N, 102, 256]	[N, 102, 256]
Layer2	Dense	256	[N, 102, 256]	[N, 102, 256]
Activation	LeakyReLU	0.1	[N, 102, 256]	[N, 102, 256]



Layer3	Dropout	0.2	[N, 102, 256]	[N, 102, 256]
Recurrent input				
Layer4	LSTM	128	[N, 102, 256]	[N, 102, 128]
Layer5	Dense	128	[N, 102, 128]	[N, 102, 128]
Activation	LeakyReLU	0.1	[N, 102, 128]	[N, 102, 128]
Layer6	Dense	64	[N, 102, 128]	[N, 102, 64]
Activation	LeakyReLU	0.1	[N, 102, 64]	[N, 102, 64]
Layer7	Dense	32	[N, 102, 64]	[N, 102, 32]
Activation	LeakyReLU	0.1	[N, 102, 32]	[N, 102, 32]
Layer8	Dense	8	[N, 102, 32]	[N, 102, 8]
Activation	LeakyReLU	0.1	[N, 102, 8]	[N, 102, 8]
Layer9	Dropout	0.2	[N, 102, 8]	[N, 102, 8]
Layer10	Dense	1	[N, 102, 8]	[N, 102, 1]

139

140

141

## 142 **2.2 Rupture scenarios and synthetic waveforms**

143 The Chilean Subduction Zone on the west coast of South America is nearly 3000 km long and  
144 accommodates 78-85mm/yr of convergence between the Nazca and South American plates  
145 (DeMets et al., 2010). It regularly hosts large magnitude earthquakes including five Mw7.6+  
146 events in the last 10 years (Riquelme et al., 2018). Chile has a real-time HR-GNSS network with  
147 more than 120 stations currently in operation (Báez et al., 2018), and provides an excellent  
148 testbed for our proposed approach.

149

150 For generating the kinematic ruptures we use the Slab2.0 3D slab geometry of (Hayes et  
151 al., 2018). We utilize the Chilean slab model from its southern terminus to ~100 km north of the

152 Chile/Peru border. We limit the seismogenic depth to 55 km consistent with the down-dip extent  
153 of recently observed large earthquakes (Ruiz & Madariaga, 2018). The resulting geometry spans  
154 a nearly 3000 km long, and 200 km wide fault. The entire fault is then gridded into a total of 3075  
155 triangular subfaults using a finite element mesher, the average length and width of the subfault  
156 vertices is ~12 km.

157

158 From this global megathrust geometry we generate the 27,200 ruptures (Figure S1) which span  
159 the magnitude range Mw7.4 to Mw9.6 using the stochastic approach first described by Graves &  
160 Pitarka (2010) with modifications proposed by LeVeque et al., (2016) to avoid the use of Fourier  
161 transformations. The magnitudes of the scenarios are uniformly distributed; we generate the same  
162 number of earthquakes for each magnitude bin. The goal here is not to obey the Guttenberg-  
163 Richter frequency magnitude distribution but rather to generate a meaningful large and varied  
164 number of ruptures to expose M-LARGE to a sufficient variety of sources. The process of  
165 generating one particular rupture and its associated waveforms is described in detail in Melgar et  
166 al. (2016) and is summarized here: once the target magnitude is selected, we define the length  
167 and width of fault for that particular rupture. We make a random draw from a probabilistic length,  
168  $L$ , and width,  $W$ , scaling law (Blaser et al., 2010).  $L$  and  $W$  are obtained from a random draw  
169 from the lognormal distributions

170

$$171 \quad \log(L) \sim N(-2.37 + 0.57M_w, \sigma_L), \quad (1)$$

172

$$173 \quad \log(W) \sim N(-1.86 + 0.46M_w, \sigma_W), \quad (2)$$

174

175 with standard deviations defined in the original work of Blaser et al. (2010). The objective is to  
176 obtain a length and width that is consistent with the behavior seen in earthquakes worldwide while  
177 retaining the observed variability as well. The probabilistic scaling law thus ensures that for a

178 given magnitude we do not always employ the same fault dimensions. Detailed statistics on the  
179 resulting fault dimensions for all simulated ruptures can be seen in [Figure S1](#). Once the fault  
180 dimensions are defined, we select a location on the megathrust at random to locate this rupture  
181 on. This also promotes larger source complexity due to larger variation of the hypocenter-centroid  
182 separation for large events ([Figure S4](#)). Here we do not take into account the variability in along-  
183 strike plate convergence rates or any information pertaining to which parts of the megathrust are  
184 considered more or less likely to experience a rupture. Rather, as with the magnitude definition,  
185 by keeping a uniform probability across the megathrust we are simply attempting to generate a  
186 diverse enough set of ruptures to expose the machine learning algorithm to.

187

188 Having selected the portion of megathrust we next generate the slip pattern and GNSS  
189 waveforms. For this we use the Karhunen-Loeve (KL) expansion method ([LeVeque et al., 2016](#),  
190 [Melgar et al., 2016](#));). The process is separated into the following three main steps: 1) generate  
191 the stochastic slip patterns, 2) define rupture kinematics, and 3) forward synthesis of GNSS  
192 waveforms using a Green's function approach. Detailed processes are provided in the Text S1 in  
193 the supporting information. Finally, to make the synthetic data more realistic, we introduce noise  
194 into the displacement waveform characteristics using a known real-time GNSS noise model  
195 ([Melgar et al., 2020](#)) which was computed from analysis of one year-long real HR-GNSS  
196 observations spanning a large region. The reference noise model provides expected spectra of  
197 noise that vary from the 1st percentile or "low" noise model, continuously through the 50th  
198 percentile "median" noise model and up to the 90th percentile "high" noise model. For each  
199 waveform we randomly select the percentile noise model and add it to the displacement data. It's  
200 worthwhile noting that we only assume the amplitude spectrum of noise, we keep the phase  
201 spectrum random. This guarantees that for a specific noise amplitude model the resulting time-  
202 domain waveform varies with each realization. In this way we guarantee a large variability of noise  
203 and quality in the stations as is routinely seen in true real-time operations.

204

205 To ensure that the waveforms are realistic, we validate the HR-GNSS by comparing the  
206 simulated peak ground displacement against what is expected from PGD-Mw scaling (Melgar et  
207 al., 2015; Ruhl et al., 2019). This is shown in Figure S5, we find that the synthetic PGD pattern  
208 matches the scaling based on real observations at hypocentral distance ~100 km and Mw from  
209 Mw7.7 to Mw8.7. We note that misfit between modeled and expected values of PGD increases  
210 at Mw greater than Mw9.0 or hypocentral distance smaller than 10km. This has been noted before  
211 in Melgar et al. (2016) and is due to the fact that the PGD regressions are constructed from  
212 databases of real events; large earthquakes (i.e. Mw9.0+) and very close observations are  
213 comparatively rare in those databases. The larger misfit is also due to the point source assumption  
214 in PGD-Mw scaling laws. All the resulting synthetic data is publicly available on Zenodo  
215 (<https://zenodo.org/record/4008690>) (Lin et al., 2020).

216

### 217 **2.3 M-LARGE: PGD features and Mw labeling**

218 To rapidly determine Mw in real time, we train M-LARGE by linking the input PGD time series  
219 recorded at each GNSS station to the time dependent Mw for each rupture derived from  
220 integration of the source time function (STF). PGD time series is calculated from

221

$$222 \quad PGD(t) = \max(\sqrt{E(t)^2 + N(t)^2 + Z(t)^2}), \quad (3)$$

223

224 where  $E(t)$ ,  $N(t)$ ,  $Z(t)$  represents the East, North and vertical component of the GNSS  
225 displacement time series starting from the earthquake origin (i.e.  $t=0$ ), respectively. We introduce  
226 feature scaling, which is commonly applied in machine learning, to avoid large feature values  
227 dominating smaller ones, making the model convergence difficult. The PGD time series is first  
228 clipped at a minimum of 0.02m and scaled logarithmically. This is done so that during this re-

229 scaling process the zero-valued data do not diverge to negative infinity. We add an additional  
230 “station existence” feature channel for every station to distinguish the difference between a very  
231 small value and no data from a simulated station outage. We set the code to zero to simulate a  
232 station malfunction due to an outage, and set it to 0.5 if the station is working normally. We  
233 decimate all the time series to 5 second sampling so that we obtain Mw updates in 5 second  
234 increments. A total of 121 stations ([Figure 1](#)) with their corresponding existence codes, and 102  
235 time steps (i.e. 5 s sampling for 510 s of signal duration) of data are used. Data incompleteness  
236 is included by randomly removing stations up to a maximum of 115 stations (i.e. a minimum of  
237 only 6 stations remaining). We also set a minimum threshold so that at least 4 stations are located  
238 within 3 degrees from the hypocenter. This is to make sure that the removal of training data still  
239 carries some near-field information, otherwise the algorithm may introduce a bias because of the  
240 similar far-field values but different labeled magnitudes. Note that the hypocenter is the only  
241 necessary information for data augmentation. During the training process, no hypocenter  
242 information is needed. Here we also note that M-LARGE does not detect the onset of an event.  
243 GNSS data is noisy enough that event detection from the real-time data can lead to many false  
244 positives ([Kawamoto et al., 2016](#)). Rather M-LARGE requires triggering, ostensibly by a seismic  
245 system as is common in other GNSS algorithms (e.g. [Crowell et al., 2018](#)). The noise in GNSS  
246 data is greater than that in seismic data and many algorithms have been demonstrated for  
247 detection of the onset of events using inertial recordings ([Perol et al., 2018](#); [Ross et al., 2018](#);  
248 [Zhu & Beroza, 2019](#)) so a system that relies on seismometers for triggering is still the most robust.

249

250 For the Mw labeling, we use the time integration from the real STF, convert it to the moment  
251 magnitude scale, and re-scale this by dividing the resulting value by 10 for computational  
252 efficiency. One assumption we have made is that there is no travel time delay due to the  
253 propagation of seismic waves from source-to-station in the feature and label pair. Although the  
254 feature and the Mw label should theoretically have a delay term, we consider this a neglectable

255 misfit in the model. In fact, the misfit is only a small portion at the beginning of the sequence  
256 considering the whole 510 s of long time series, and the algorithm seems to address this properly  
257 to predict the non-delayed label after more incoming data are available. This non-delayed  
258 prediction continues until the rupture termination and information has completely propagated to  
259 stations when the real data and Mw label synchronize with each other.

260

## 261 **2.4 GFAST and GPSCMT**

262 Our main point of comparison for assessing whether M-LARGE is an improvement will be  
263 GFAST ([Crowell et al., 2016](#)), which is one of the most stable GNSS EEW methods and is  
264 currently operating in the U.S. EEW system (i.e. ShakeAlert). It uses the PGD observations from  
265 HR-GNSS time series. When a hypocenter is confirmed by a seismic method, the magnitude is  
266 calculated based on the PGD-Mw scaling relationship ([Crowell et al., 2016](#); [Melgar et al., 2015](#);  
267 [Ruhl et al., 2019](#)). To ensure the data contain PGD information and not noise, a 3 km/s travel-  
268 time filter is added into the algorithm, and the model only predicts Mw when at least 4 stations  
269 have valid information.

270 GFAST is not the only GNSS modeling approach, there are other proposed algorithms that  
271 utilize near-field GNSS data to rapidly estimate earthquake magnitude. To further compare with  
272 M-LARGE we also run the Global Positioning System based centroid moment tensor (GPSCMT)  
273 method, which utilizes the near-field static offset term from the GNSS records to calculate  
274 magnitude, moment tensor and centroid location ([Melgar et al., 2012](#); [Lin et al., 2019](#)). Unlike the  
275 GFAST approach, GPSCMT does not require hypocenter information, instead it grid-searches  
276 every pre-built centroid location, solves for the moment tensor and finds the preferred location  
277 which has the minimum residual. We take the same subfault meshes used by M-LARGE, used to  
278 generate rupture scenarios, as the potential centroid locations. Both the performance of GFAST  
279 and GPSCMT are shown in the next section.

280

## 281 **3 Results**

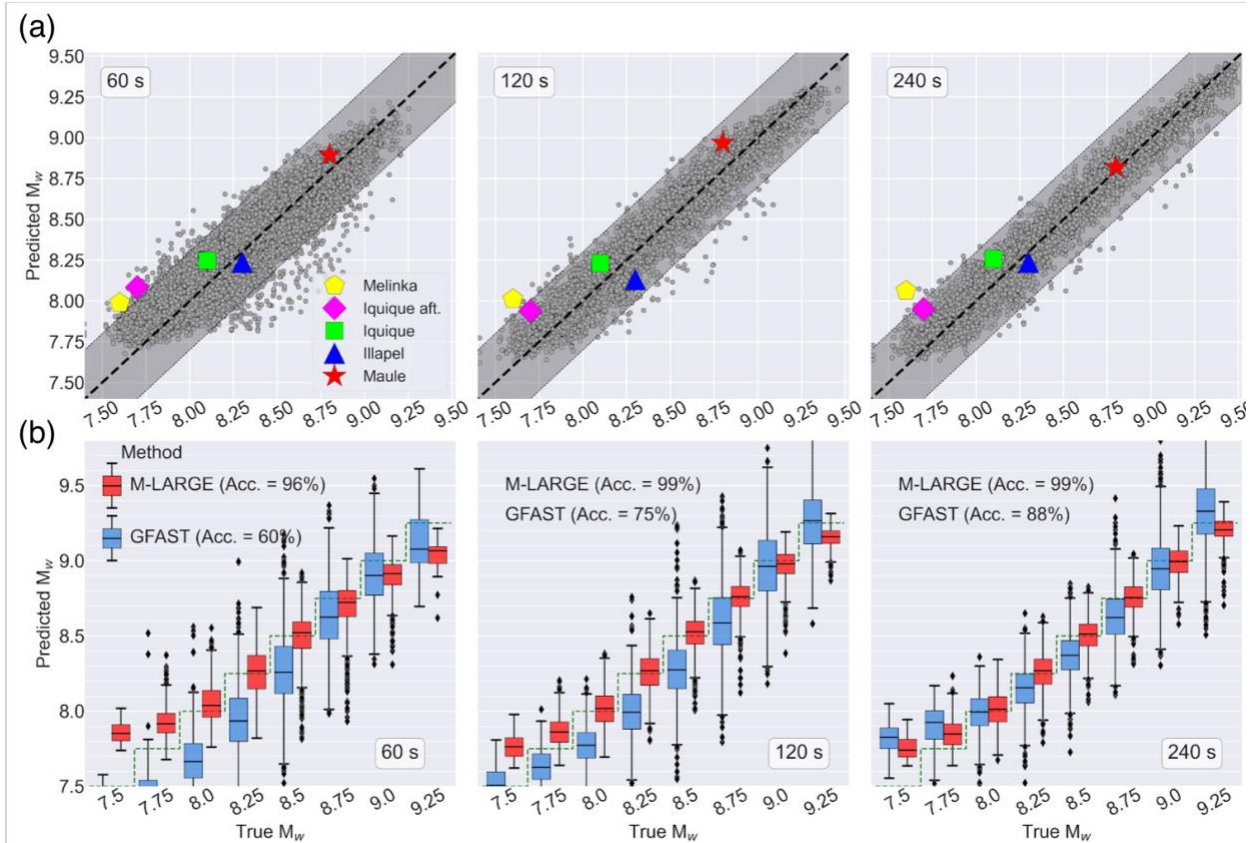
### 282 **3.1 M-LARGE performance on testing dataset**

283 The performance of M-LARGE on the testing dataset is shown in [Figure 3](#). We define a correct  
284 prediction as one within  $\pm 0.3$  units of the target magnitude (i.e. time-dependent magnitude) and  
285 calculate the model accuracy ([Figure 3b](#), [Figure S6a](#) in the supporting information). Within these  
286 bounds, the model performs well with a high accuracy of 96% after 60 s which increases to 99%  
287 by 120 s. The standard deviation of the magnitude misfits are 0.14, 0.1, 0.09 at 60, 120, and 240  
288 s, respectively. We compare this statistic to the GFAST algorithm by using the same testing  
289 dataset as M-LARGE. Note that for GFAST, we remove those predictions with  $M_w=0$  due to the  
290 four station minimum thresholding and only show the data that have predicted values ([Figure 3b](#)).  
291 Despite this, we find that GFAST has a longer determination time and lower accuracy of 60% at  
292 60 s which slowly increases to 88% by 240 s. In comparison to M-LARGE, GFAST's accuracy  
293 saturates at 88.1% by 255 seconds. The standard deviation of the magnitude predictions of  
294 GFAST are also larger 0.23, 0.19, 0.18 at 60, 120, 240 s, respectively, about 2 times more scatter  
295 than the M-LARGE performance. To summarize, M-LARGE reaches 80% accuracy 5 times faster  
296 than GFAST and has half the scatter on average.

297 Furthermore, we compare the performance between M-LARGE and the GPSCMT ([Figure S7](#)).  
298 Again, M-LARGE significantly outperforms the GPSCMT, where the accuracies are 40%, 25%  
299 and 24% at 60, 120, 240 s, respectively. Noting that the GPSCMT performs with overall much  
300 larger scatter, lower accuracy, and systematic overestimations. This has been noted before, that  
301 a point source has limited ability on recovering the deformation of large offshore events (e.g.  
302 [Melgar et al., 2013](#)). Thus, without additional constraints, the model accuracy of GPSCMT method  
303 is about 40% according to our testing dataset.

304

305



306

307 **Figure 3.** Model performance on testing dataset and on real events. (a) (from left to right) snapshots of the  
 308 M-LARGE performance at 60, 120, 240 s, respectively. Gray dots show the  $M_w$  predictions compared to  
 309 the time-dependent magnitude. Black dashed line represents the 1:1 line; shaded area represents the  
 310  $\pm 0.3$  magnitude range. Colored markers denote the M-LARGE predicted  $M_w$  and their final  $M_w$  for 5 real  
 311 events in Figure 1. (b) comparison of the GFAST (blue) and M-LARGE (red) predicted magnitudes at  
 312 60, 120 and 240 s for different magnitude bins. Model accuracies at 60, 120 and 240 s are shown in text.  
 313 The green dashed line is the 1:1 reference for each magnitude bin.

314

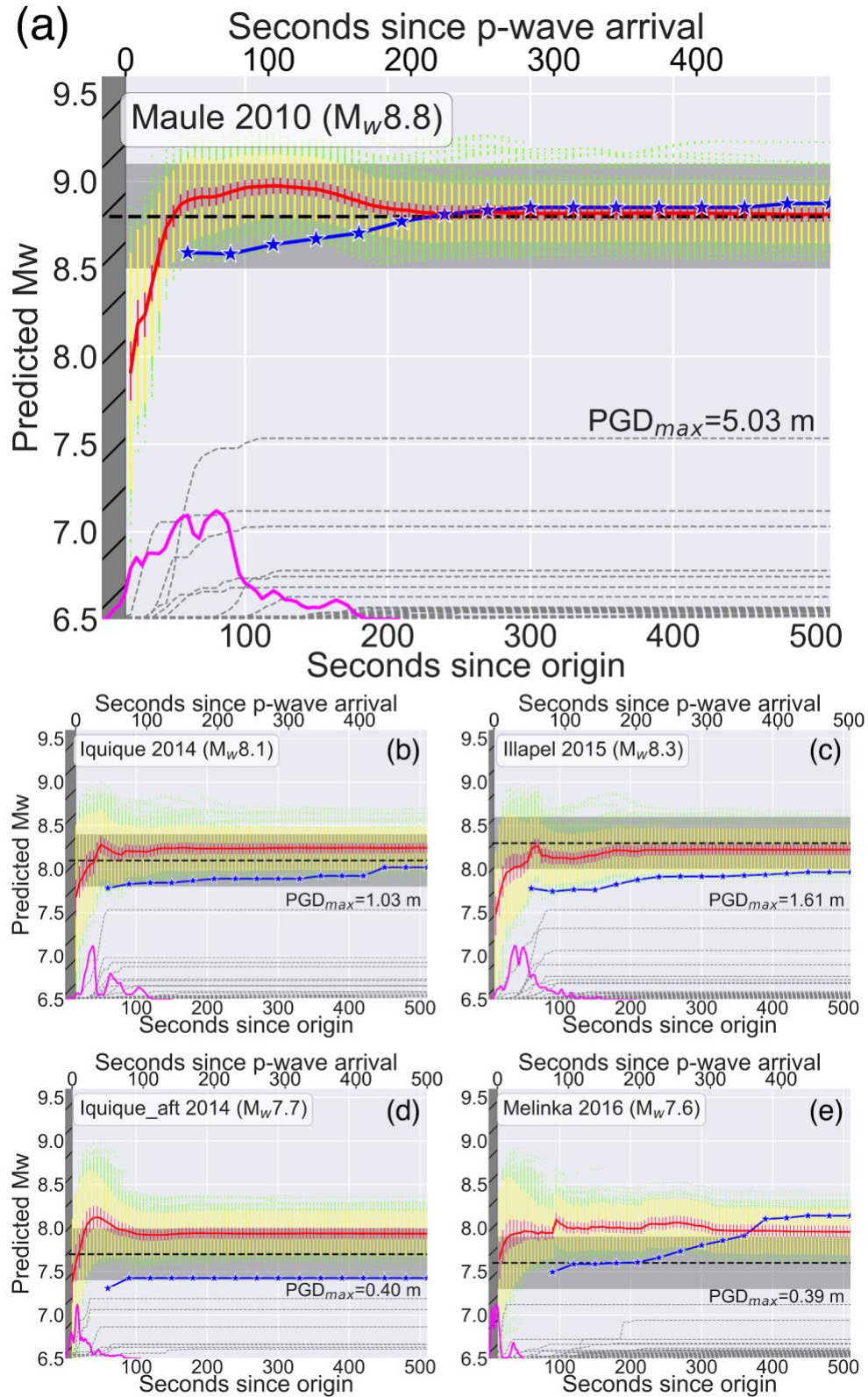
315

### 316 3.2 M-LARGE performance on real large earthquakes

317 To further assess the performance of M-LARGE, we apply the model to five large historical  
 318 events in the Chilean Subduction Zone with HR-GNSS records which are not employed in training  
 319 (Figure 4). For each of these earthquakes different numbers of GNSS sites were available. For



320 the 2010 Mw8.8 Maule earthquake the model only takes 40 s to reach the +/-0.3 magnitude unit  
321 criteria. M-LARGE also successfully predicts the final magnitude of the 2014 Mw8.1 Iquique and  
322 the 2015 Mw8.3 Illapel earthquakes at 20 s and 35 s, respectively. For the 2014 Mw7.7 Iquique  
323 aftershock and the 2016 Mw7.6 Melinka earthquakes, the M-LARGE predictions both overshoot  
324 the true magnitude at 30 s, but soon correct downward. We also note that the performance  
325 statistics are quoted from the event origin time and include delay times prior to the P-wave arrival  
326 at the closest stations. In most events the first arrival occurs by 20 s, and only 6% of rupture  
327 scenarios have arrivals later than 20 s. For the Maule earthquake, where most of the presently  
328 operating closest stations did not exist, the first arrival times are 17 s. Considering these delay  
329 times, useful predictions are made as soon as the signals are recorded but the lowest  
330 uncertainties are anticipated after ~30 s. This can be seen in [Figure 4](#) and [Figure S6](#), where lower  
331 uncertainties occur in the later predictions.



332

333 **Figure 4.** M-LARGE performance on real Chilean earthquakes. (a) The 2010 Maule  $M_w 8.8$  earthquake.

334 Black dashed line and gray shaded areas represent the true  $M_w$  and the  $\pm 0.3$  magnitude unit range. Red

335 *line shows the M-LARGE predicted  $M_w$ , with the boxes (red bars) and whiskers (yellow bars) denoting the*  
336 *50% and 99.7% of the target  $M_w$  population, respectively. Green dots represent outliers. Blue stars show*  
337 *the GFAST prediction given the same data used by M-LARGE. Thin dashed lines show the PGD waveforms*  
338 *from the GNSS network (Figure 1). Magenta line represents the event source time function from the USGS*  
339 *finite fault. Hatched dark gray area is the time period prior to the arrival of the P-wave at the closest site*  
340 *where no information on the rupture is available. (b)-(e) Same as (a) but for the 2014  $M_w$ 8.1 Iquique*  
341 *earthquake, the 2015  $M_w$ 8.3 Illapel earthquake, the 2014  $M_w$ 7.7 Iquique aftershock, and the 2016  $M_w$ 7.6*  
342 *Melinka earthquake, respectively.*

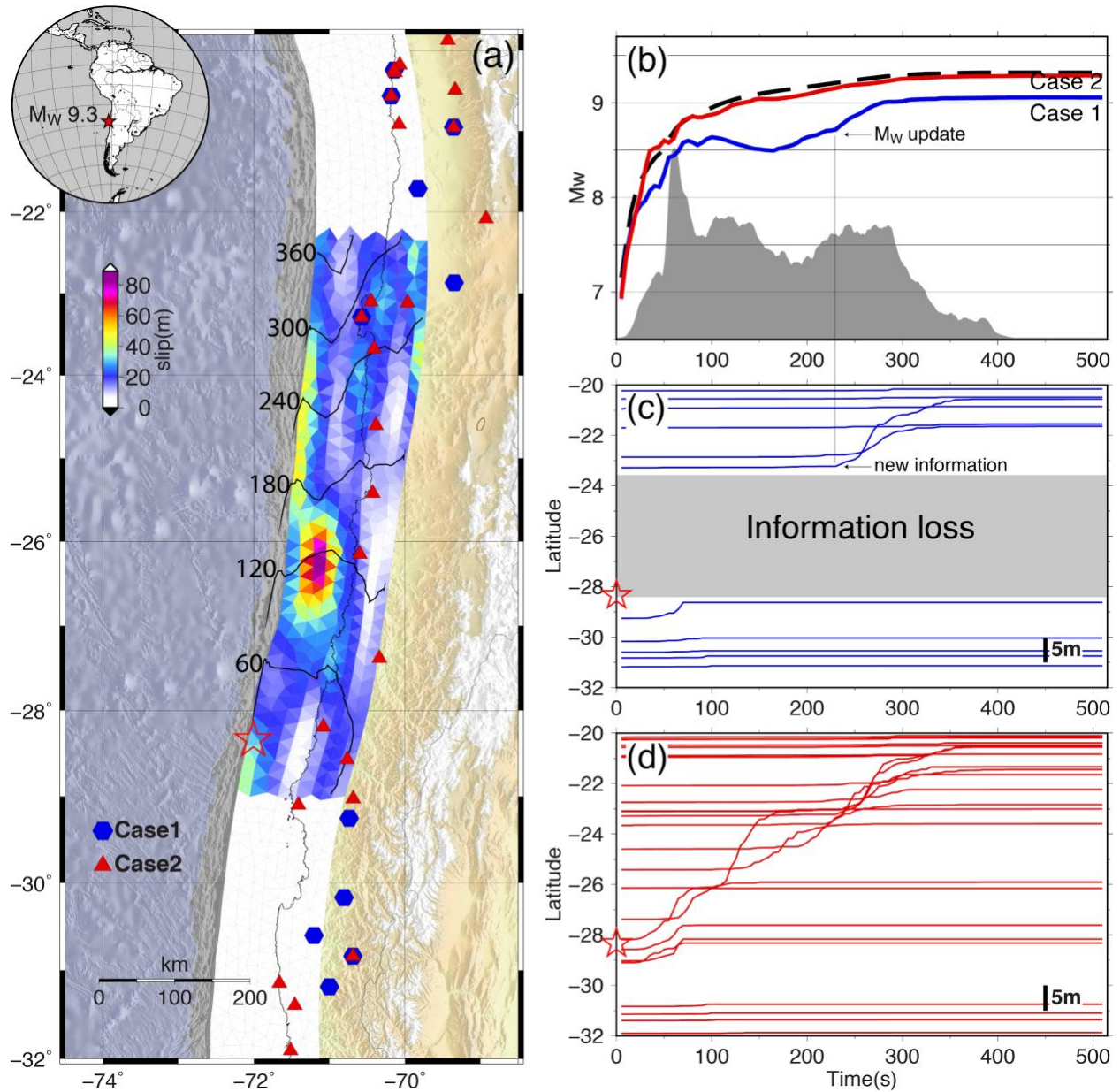
343

344

### 345 **3.3 M-LARGE performance on imperfect data**

346 Given the limited availability of real events, it is important to investigate how M-LARGE  
347 performs on imperfect data. First, we test the M-LARGE on two different recording scenarios on  
348 the same rupture with one having poor station coverage versus well coverage for the other one  
349 (Figure 5). In the poor station coverage example (i.e. Case 1 in Figure 5), almost all the near-field  
350 data are missing and M-LARGE is only able to successfully estimate magnitude after 230 s, when  
351 far field stations begin recording data and M-LARGE upgrades its moment estimate (Figure 5b,  
352 5c). In contrast, in the second example, abundant near-field data is used to accurately  
353 characterize the rupture process and M-LARGE predicts the actual magnitude in 120 s (Figure  
354 5b, 5d). This suggests that data sparsity in the near-field plays the most important role for the  
355 accuracy and timeliness of the predictions. The clear implication is that having more stations  
356 closer to the source improves M-LARGE's performance.

357



358

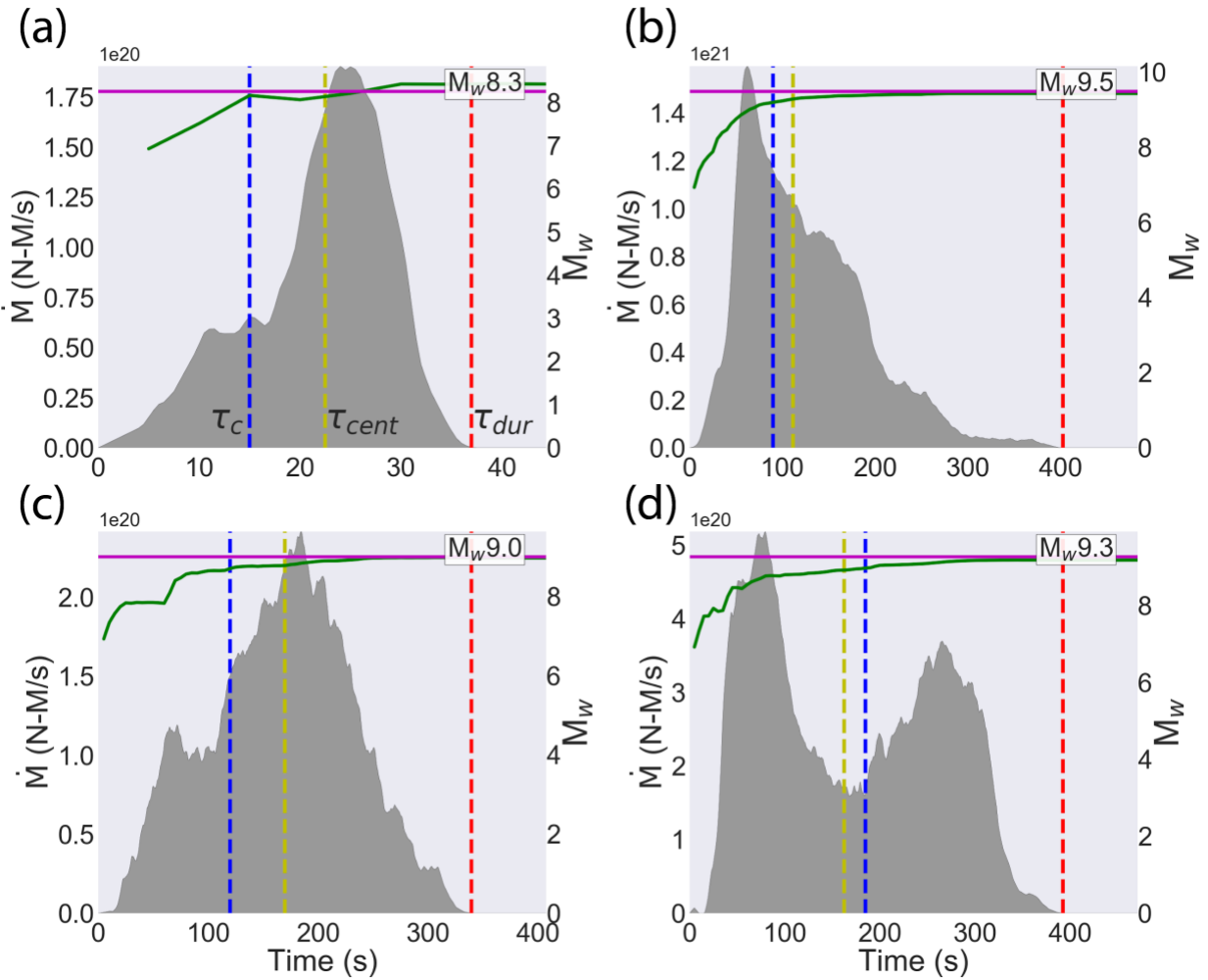
359 **Figure 5.** M-LARGE prediction tests with different station distributions. (a) rupture scenario of a Mw9.3  
 360 earthquake with the station distribution of Case1 (blue hexagon) and Case2 (red triangle). Black lines with  
 361 numbers show the rupture time contours. (b) M-LARGE predictions for Case 1 (blue line), Case 2 (red line)  
 362 and the actual Mw (dashed line) calculated from the STF (gray area). (c) PGD data of Case 1 sorted by  
 363 latitude, Red star denotes the hypocenter latitude. (d) similar to (c), but data of Case 2.

364

365

366 **3.4 M-LARGE performance on different source time function types**

367 To examine the M-LARGE performance as a function of source complexity, we choose four  
 368 different characteristic source time function shapes (i.e. symmetric, bimodal, early and late  
 369 skewed) and analyze the results. Figure 6 shows examples of each of these characteristic STFs,  
 370 we find that the complexity of the time dependent moment evolution does not affect the accuracy  
 371 of the M-LARGE estimations because it is trained to map the actual STF directly.



372  
 373 **Figure 6.** Example plot for the  $\tau_c$ (time to corrected prediction),  $\tau_{cent}$ (centroid time),  $\tau_{dur}$ (duration). Green  
 374 and magenta line shows the M-LARGE prediction and final magnitude, respectively. (a) shows the case of  
 375 late rupturing, where the source focuses at the end of the rupture. (b) shows the case with early rupturing,  
 376 where the source focuses at the beginning of the rupture. (c) nearly symmetric (triangular) source time  
 377 function. (d) shows the case of two rupture asperities.

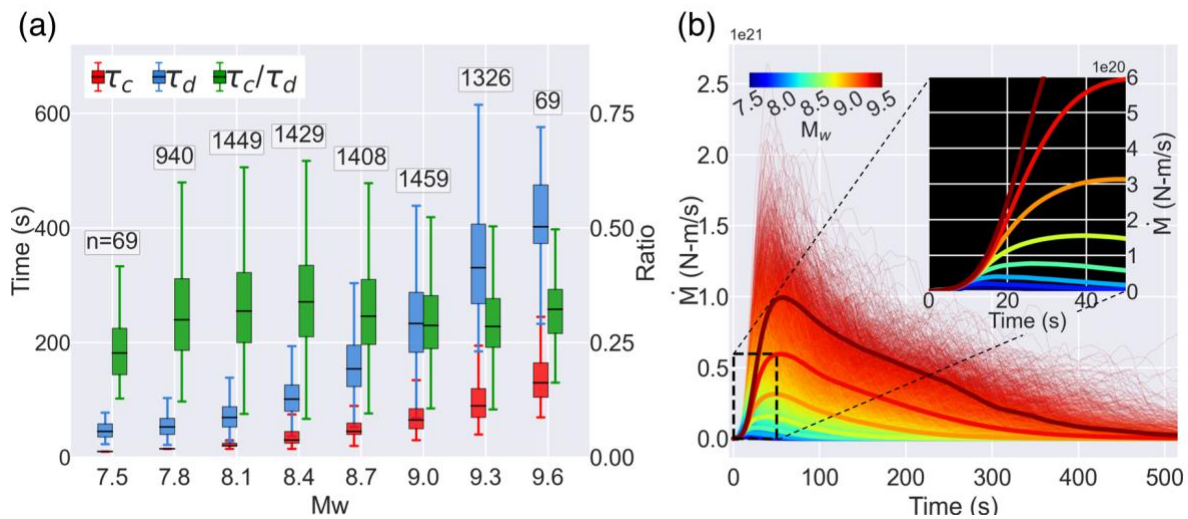
378

## 379 **4. Discussion**

### 380 **4.1 Earlier final magnitude estimation**

381 Although the timeliness of the final magnitude assessment is intimately tied to the evolution of  
382 the STFs (i.e. whether the event grows faster or slower), we find that the final magnitude can, on  
383 average, still be predicted by 20%-40% of the rupture duration time (Figure 7a). This earlier  
384 prediction of M-LARGE is in part due to our definition of correct prediction (i.e. +/-0.3 magnitude  
385 unit). Based on the Mw-duration scaling of Duputel et al. (2013), an -0.3 magnitude unit  
386 earthquake can be estimated by 71% of the original duration time (a detailed derivation is provided  
387 in the Test S2 in the supporting information). For example, on average, a Mw9.0 event takes ~170  
388 s to rupture, while it only takes 120 s to rise to the acceptable Mw threshold of Mw8.7. In this  
389 case, a final prediction can be made before the rupture termination providing a shortcut to practical  
390 warning, and this is only possible when the real-time STF can be accurately measured. However,  
391 this only accounts for 71 % of the original duration. Additionally to explain the faster magnitude  
392 estimation time, which is 20%-40% of duration, we find that the M-LARGE's real-time STF is likely  
393 leveraging some degree of the weak determinism (Meier et al., 2017; Goldberg et al., 2018;  
394 Melgar & Hayes, 2019) that is present, on average, in the training data and in the Chilean events  
395 used for final validation. For example, the Mw8.8 Maule earthquake converges to its correct  
396 magnitude even before the peak moment rate in the source time function (Figure 4a) and the  
397 duration of the acceptable +/-0.3 Mw range (i.e. Mw8.5 takes ~95 s to rupture). When exactly,  
398 during the rupture process, final earthquake magnitude can be determined is still debated in the  
399 earthquake science community. The end member views are that earthquakes are strongly  
400 deterministic (Wu & Zhao, 2006; Olson & Allen, 2005), i.e. information about the final magnitude  
401 is contained in the signals from the first seconds following nucleation of the event; and that they  
402 are not deterministic at all (Rydelek & Horiuchi, 2006; Ide, 2019), i.e. magnitude cannot be  
403 determined before the rupture is complete. We note here that we have not explicitly assumed

404 any determinism in the generation of our synthetic rupture scenarios used to train M-LARGE.  
 405 Instead, our training models have growth patterns that behave according to what is seen in  
 406 worldwide databases (Figure 7b). That said, any individual rupture scenario may depart from this  
 407 average behavior (i.e. see Figure S8 in the supporting information) and ultimately the success of  
 408 M-LARGE is contingent on how representative the training data is of real large magnitude  
 409 earthquakes. In sum, the model learns some degree of determinism of the earthquake source,  
 410 facilitating faster final magnitude prediction.  
 411



412 **Figure 7.** Warning time ratios and STF analysis. (a) shows the duration ( $\tau_d$ ), time to the correct prediction  
 413 ( $\tau_c$ ), and the ratio between these two for each magnitude bin. Texts indicate the number of samples for  
 414 each bin. (b) shows the STF of 27200 rupture scenarios color coded by  $M_w$ . Thick lines denote the averaged  
 415 STF of different magnitude bins. Inset shows the zoom-in view of the averaged source time functions.  
 416

417

418

## 419 4.2 Limitations and future steps

420 We have shown that M-LARGE has the ability to learn complex rupture patterns from the crustal  
 421 deformation data. Also, that it significantly outperforms other HR-GNSS algorithms. However, we  
 422 note that it still has some limitations and these should be targets for potential improvements in

423 the future. First, once M-LARGE is trained, the model is not global in scope, it is limited by the  
424 simulated earthquakes and waveforms for a particular region (i.e. in this study, the Chilean  
425 Subduction Zone). Thus, the model needs to be re-trained to adapt to different areas. Although  
426 the model can be generalized by introducing feature engineering (e.g. extract the hypocentral  
427 distance used by GFAST), we have not attempted to generalize it because regional heterogeneity  
428 such as site effects, subduction zone environments and station distribution vary, so global model  
429 generalization is non-trivial. However, synthesis of the ruptures and GNSS waveforms is fast  
430 enough that re-training for another network or region is not a numerically prohibitive task. Second,  
431 we note that for the 2010 Mw8.8 Maule earthquake example, there is a 17 s gap without recording  
432 due to lack of near-field stations. This performance could be sped up by ~10 s if the information  
433 delay introduced by the travel times could be reduced, i.e. if station coverage could be expanded  
434 offshore.

435 We note that the model architecture and hyperparameters are selected arbitrarily and the scale  
436 of hyperparameters are comparable to the similar studies (e.g. [Ross et al., 2018](#); [Zhu & Beroza,](#)  
437 [2019](#)). Beside the architecture we used ([Figure 2](#)), we have also explored the parameter space.  
438 However, we do not find significant model improvement on tuning the hyperparameters, probably  
439 because the model has already reached its accuracy limit (i.e. 99%) based on the currently  
440 designed architecture. Any further improvement will need more delicate model design. We find  
441 that the logarithm scaling function of PGD features has better performance against the commonly  
442 adopted linear scaling. This is consistent with the existence of logarithm PGD and magnitude  
443 relationships ([Crowell et al., 2016](#); [Melgar et al., 2015](#); [Ruhl et al., 2019](#)) making the input and  
444 output pairs less complicated during model training.

445 The earthquake magnitude is not the only important factor for EEW. In fact, the source location,  
446 rupture length and width are equally important for an accurate ground motion prediction or  
447 tsunami amplitude forecast. In this paper, we have successfully demonstrated that M-LARGE is  
448 capable of learning Mw directly from raw observations. This is a starting point for this new type of



449 I EEW algorithm, and we anticipate that, given this success, it is reasonable to infer that M-LARGE  
450 can be expanded to learn other source parameters necessary for hazards forecasts.

451

452

## 453 **5 Conclusion**

454 Developing frameworks to provide timely warning during the largest magnitude earthquakes  
455 remains an outstanding scientific and technological challenge. EEW systems continue to expand  
456 and have proliferated to many countries across the globe (Allen & Melgar, 2019). Despite this,  
457 how these systems will perform in rare but high consequence, large magnitude earthquakes is  
458 uncertain. Here, we have combined knowledge of where great earthquakes will occur, their  
459 average expected rupture characteristics, state of the art sensor technology, and deep learning  
460 to rapidly characterize large magnitude earthquakes from their crustal deformation patterns. The  
461 resulting EEW algorithm, M-LARGE, has significantly better performance than current algorithms  
462 and can readily be generalized to any faulting environment capable of generating large events.  
463 As such, M-LARGE represents a new approach to EEW that if made operational, will obviate  
464 many of the performance limitations of current technologies providing accurate and fast alerts that  
465 will lead to increased resilience.

466

467

## 468 **Data availability**

469 The rupture simulations and waveforms can be found on Zenodo:  
470 <https://zenodo.org/record/4008690> (Lin et al., 2020). The code of M-LARGE can be obtained at  
471 <https://zenodo.org/record/4527253> (Lin, 2021).

472

## 473 **Acknowledgement**

474 This work is funded by National Aeronautics and Space Administration NESSF grant  
475 80NSSC18K1420 and National Science Foundation grants 1663834 and 1835661. This work is  
476 also partially funded by NASA grants 80NSSC19K0360 and 80NSSC19K1104. We thank the  
477 Centro Sismologico Nacional of Chile for operation of the HR-GNSS network and access to their  
478 data. We would also like to thank Amy Williamson and Brendan Crowell for discussions on the  
479 performance of GFAST on simulated events.

480

## 481 **References**

482

483 Allen, R. M., & Melgar, D. (2019), Earthquake early warning: Advances, scientific challenges,  
484 and societal needs. *Annual Review of Earth and Planetary Sciences*, 47, 361-388.

485

486 Báez, J. C., Leyton, F., Troncoso, C., del Campo, F., Bevis, M., Vigny, C., ... & Blume, F. (2018),  
487 The Chilean GNSS network: Current status and progress toward early warning applications.  
488 *Seismological Research Letters*, 89(4), 1546-1554.

489

490 Blaser, L., Krüger, F., Ohrnberger, M., & Scherbaum, F. (2010), Scaling relations of earthquake  
491 source parameter estimates with special focus on subduction environment. *Bulletin of the*  
492 *Seismological Society of America*, 100(6), 2914-2926.

493

494 Bock, Y., & Melgar, D. (2016), Physical applications of GPS geodesy: A review. *Reports on*  
495 *Progress in Physics*, 79(10), 106801.

496

497 Boore, D. M., & Bommer, J. J. (2005). Processing of strong-motion accelerograms: needs, options  
498 and consequences. *Soil Dynamics and Earthquake Engineering*, 25(2), 93-115.

499

500 Böse, M., Heaton, T. H., & Hauksson, E. (2012), Real-time finite fault rupture detector (FinDer)  
501 for large earthquakes. *Geophysical Journal International*, 191(2), 803-812.

502

503 Cochran, E. S., Bunn, J., Minson, S. E., Baltay, A. S., Kilb, D. L., Kodera, Y., & Hoshihara, M.  
504 (2019), Event Detection Performance of the PLUM Earthquake Early Warning Algorithm in  
505 Southern California. *Bulletin of the Seismological Society of America*, 109(4), 1524-  
506 1541.

507

508 Colombelli, S., Allen, R. M., & Zollo, A. (2013), Application of real-time GPS to earthquake early  
509 warning in subduction and strike-slip environments. *Journal of Geophysical Research: Solid*  
510 *Earth*, 118(7), 3448-3461.

511

512 Crowell, B. W., Melgar, D., Bock, Y., Haase, J. S., & Geng, J. (2013), Earthquake magnitude  
513 scaling using seismogeodetic data. *Geophysical Research Letters*, 40(23), 6089-6094.

514

515

516 Crowell, B. W., Schmidt, D. A., Bodin, P., Vidale, J. E., Gomberg, J., Renate Hartog, J., ... &  
517 Jamison, D. G. (2016), Demonstration of the Cascadia G-FAST geodetic earthquake early  
518 warning system for the Nisqually, Washington, earthquake. *Seismological Research Letters*,  
519 87(4), 930-943.  
520  
521 Crowell, B. W., Schmidt, D. A., Bodin, P., Vidale, J. E., Baker, B., Barrientos, S., & Geng, J.  
522 (2018). G-FAST earthquake early warning potential for great earthquakes in Chile. *Seismological  
523 Research Letters*, 89(2A), 542-556.  
524  
525 DeMets, C., Gordon, R. G., & Argus, D. F. (2010), Geologically current plate motions. *Geophysical  
526 Journal International*, 181(1), 1-80.  
527  
528 Duputel, Z., Tsai, V. C., Rivera, L., & Kanamori, H. (2013). Using centroid time-delays to  
529 characterize source durations and identify earthquakes with unique characteristics. *Earth and  
530 Planetary Science Letters*, 374, 92-100.  
531  
532 Frankel, A., Wirth, E., Marafi, N., Vidale, J., & Stephenson, W. (2018), Broadband Synthetic  
533 Seismograms for Magnitude 9 Earthquakes on the Cascadia Megathrust Based on 3D  
534 Simulations and Stochastic Synthetics, Part 1: Methodology and Overall Results Methodology and  
535 Overall Results. *Bulletin of the Seismological Society of America*, 108(5A), 2347-2369.  
536  
537 Geng, J., Pan, Y., Li, X., Guo, J., Liu, J., Chen, X., & Zhang, Y. (2018). Noise characteristics of  
538 high-rate multi-GNSS for subdaily crustal deformation monitoring. *Journal of Geophysical  
539 Research: Solid Earth*, 123(2), 1987-2002.  
540  
541 Glorot, X., Bordes, A., & Bengio, Y. (2011), Deep sparse rectifier neural networks. In Proceedings  
542 of the fourteenth international conference on artificial intelligence and statistics (pp. 315-323).  
543  
544 Goldberg, D. E., Melgar, D., Bock, Y., & Allen, R. M. (2018), Geodetic observations of weak  
545 determinism in rupture evolution of large earthquakes. *Journal of Geophysical Research: Solid  
546 Earth*, 123(11), 9950-9962.  
547  
548 Goldberg, D. E., Melgar, D., & Bock, Y. (2019), Seismogeodetic P-wave amplitude: No evidence  
549 for strong determinism. *Geophysical research letters*, 46(20), 11118-11126.  
550  
551 Goldberg, D. E., & Melgar, D. (2020). Generation and validation of broadband synthetic P waves  
552 in semistochastic models of large earthquakes. *Bulletin of the Seismological Society of America*,  
553 110(4), 1982-1995.  
554  
555 Grapenthin, R., Johanson, I. A., & Allen, R. M. (2014), Operational real-time GPS-enhanced  
556 earthquake early warning. *Journal of Geophysical Research: Solid Earth*, 119(10), 7944-7965.  
557  
558 Graves, R. W., & Pitarka, A. (2010), Broadband ground-motion simulation using a hybrid  
559 approach. *Bulletin of the Seismological Society of America*, 100(5A), 2095-2123.  
560  
561 Hayes, G. P. (2017), The finite, kinematic rupture properties of great-sized earthquakes since  
562 1990. *Earth and Planetary Science Letters*, 468, 94-100.  
563  
564 Hayes, G. P., Moore, G. L., Portner, D. E., Hearne, M., Flamme, H., Furtney, M., & Smoczyk, G.  
565 M. (2018), Slab2, a comprehensive subduction zone geometry model. *Science*, 362(6410), 58-  
566 61.

567  
568 Hochreiter, S., & Schmidhuber, J. (1997), Long short-term memory. *Neural computation*, 9(8),  
569 1735-1780.  
570  
571 Hoshiba, M., Iwakiri, K., Hayashimoto, N., Shimoyama, T., Hirano, K., Yamada, Y., ... & Kikuta,  
572 H. (2011). Outline of the 2011 off the Pacific coast of Tohoku Earthquake (M w 9.0)—Earthquake  
573 Early Warning and observed seismic intensity—. *Earth, planets and space*, 63(7), 547-551.  
574  
575 Hoshiba, M., & Ozaki, T. (2014), Earthquake Early Warning and Tsunami Warning of the Japan  
576 Meteorological Agency, and Their Performance in the 2011 off the Pacific Coast of Tohoku  
577 Earthquake (Mw9.0). In *Early warning for geological disasters* (pp. 1-28). Springer, Berlin,  
578 Heidelberg.  
579  
580 Hutchison, A. A., Böse, M., & Manighetti, I. (2020), Improving early estimates of large  
581 earthquake's final fault lengths and magnitudes leveraging source fault structural maturity  
582 information. *Geophysical Research Letters*, e2020GL087539.  
583  
584 Ide, S. (2019), Frequent observations of identical onsets of large and small earthquakes. *Nature*,  
585 573(7772), 112-116.  
586  
587 Kawamoto, S., Hiyama, Y., Ohta, Y., & Nishimura, T. (2016), First result from the GEONET real-  
588 time analysis system (REGARD): the case of the 2016 Kumamoto earthquakes. *Earth, Planets*  
589 *and Space*, 68(1), 190..  
590  
591 Kodera, Y., Yamada, Y., Hirano, K., Tamaribuchi, K., Adachi, S., Hayashimoto, N., ... & Hoshiba,  
592 M. (2018), The propagation of local undamped motion (PLUM) method: A simple and robust  
593 seismic wavefield estimation approach for earthquake early warning. *Bulletin of the Seismological*  
594 *Society of America*, 108(2), 983-1003.  
595  
596 Kodera, Y., Hayashimoto, N., Moriwaki, K., Noguchi, K., Saito, J., Akutagawa, J., ... & Hoshiba,  
597 M. (2020), First-Year Performance of a Nationwide Earthquake Early Warning System Using a  
598 Wavefield-Based Ground-Motion Prediction Algorithm in Japan. *Seismological Research Letters*,  
599 91(2A), 826-834.  
600  
601 Kong, Q., Trugman, D. T., Ross, Z. E., Bianco, M. J., Meade, B. J., & Gerstoft, P. (2019). Machine  
602 learning in seismology: Turning data into insights. *Seismological Research Letters*, 90(1), 3-14.  
603  
604 Larson, K. M. (2009), GPS seismology. *Journal of Geodesy*, 83(3-4), 227-233.  
605  
606 LeCun, Y., Bengio, Y., & Hinton, G. (2015), Deep learning. *nature*, 521(7553), 436-444.  
607  
608 LeVeque, R. J., Waagan, K., González, F. I., Rim, D., & Lin, G. (2016), Generating random  
609 earthquake events for probabilistic tsunami hazard assessment. In *Global Tsunami Science: Past*  
610 *and Future, Volume I* (pp. 3671-3692). Birkhäuser, Cham.  
611  
612 Lin, J. T., Chang, W. L., Melgar, D., Thomas, A., & Chiu, C. Y. (2019), Quick determination of  
613 earthquake source parameters from GPS measurements: a study of suitability for Taiwan.  
614 *Geophysical Journal International*, 219(2), 1148-1162.  
615  
616 Lin, J. T., Melgar, D., Thomas, A., & Searcy, J. (2020). Chilean Subduction Zone rupture scenarios  
617 and waveform data [Data set]. Zenodo. <http://doi.org/10.5281/zenodo.4008690>

618  
619 Lin, J. T. (2021). junting/MLARGE: First release of MLARGE (Version v1.0.0). Zenodo.  
620 <http://doi.org/10.5281/zenodo.4527253>  
621  
622 Maas, A. L., Hannun, A. Y., & Ng, A. Y. (2013), Rectifier nonlinearities improve neural network  
623 acoustic models. In Proc. icml (Vol. 30, No. 1, p. 3).  
624  
625  
626 Meier, M. A., Heaton, T., & Clinton, J. (2016), Evidence for universal earthquake rupture initiation  
627 behavior. *Geophysical Research Letters*, 43(15), 7991-7996.  
628  
629 Meier, M. A., Ampuero, J. P., & Heaton, T. H. (2017), The hidden simplicity of subduction  
630 megathrust earthquakes. *Science*, 357(6357), 1277-1281.  
631  
632 Melgar, D., Bock, Y., & Crowell, B. W. (2012), Real-time centroid moment tensor determination  
633 for large earthquakes from local and regional displacement records. *Geophysical Journal*  
634 *International*, 188(2), 703-718.  
635  
636 Melgar, D., Crowell, B. W., Bock, Y., & Haase, J. S. (2013), Rapid modeling of the 2011 Mw 9.0  
637 Tohoku-Oki earthquake with seismogeodesy. *Geophysical Research Letters*, 40(12), 2963-2968.  
638  
639 Melgar, D., Crowell, B. W., Geng, J., Allen, R. M., Bock, Y., Riquelme, S., ... & Ganas, A. (2015),  
640 Earthquake magnitude calculation without saturation from the scaling of peak ground  
641 displacement. *Geophysical Research Letters*, 42(13), 5197-5205.  
642  
643 Melgar, D., LeVeque, R. J., Dreger, D. S., & Allen, R. M. (2016), Kinematic rupture scenarios and  
644 synthetic displacement data: An example application to the Cascadia subduction zone. *Journal*  
645 *of Geophysical Research: Solid Earth*, 121(9), 6658-6674.  
646  
647 Melgar, D., & Hayes, G. P. (2017), Systematic observations of the slip pulse properties of large  
648 earthquake ruptures. *Geophysical Research Letters*, 44(19), 9691-9698.  
649  
650  
651 Melgar, D., & Hayes, G. P. (2019), Characterizing large earthquakes before rupture is complete.  
652 *Science Advances*, 5(5), eaav2032.  
653  
654 Melgar, D., Crowell, B. W., Melbourne, T. I., Szeliga, W., Santillan, M., & Scrivner, C. (2020),  
655 Noise characteristics of operational real-time high-rate GNSS positions in a large aperture  
656 network. *Journal of Geophysical Research: Solid Earth*, 125(7), e2019JB019197.  
657  
658 Minson, S. E., Murray, J. R., Langbein, J. O., & Gomberg, J. S. (2014), Real-time inversions for  
659 finite fault slip models and rupture geometry based on high-rate GPS data. *Journal of Geophysical*  
660 *Research: Solid Earth*, 119(4), 3201-3231.  
661  
662 Mousavi, S. M., & Beroza, G. C. (2020a), A machine-learning approach for earthquake magnitude  
663 estimation. *Geophysical Research Letters*, 47(1), e2019GL085976.  
664  
665 Mousavi, S. M., Ellsworth, W. L., Zhu, W., Chuang, L. Y., & Beroza, G. C. (2020b), Earthquake  
666 transformer—an attentive deep-learning model for simultaneous earthquake detection and phase  
667 picking. *Nature communications*, 11(1), 1-12.  
668

669 Murray, J. R., Crowell, B. W., Grapenthin, R., Hodgkinson, K., Langbein, J. O., Melbourne, T., ...  
670 & Schmidt, D. A. (2018), Development of a geodetic component for the US West Coast  
671 earthquake early warning system. *Seismological Research Letters*, 89(6), 2322-2336.  
672

673 Olson, E. L., & Allen, R. M. (2005), The deterministic nature of earthquake rupture. *Nature*,  
674 438(7065), 212-215 .  
675

676

677 Perol, T., Gharbi, M., & Denolle, M. (2018), Convolutional neural network for earthquake detection  
678 and location. *Science Advances*, 4(2), e1700578.  
679

680 Pitarka, A., Graves, R., Irikura, K., Miyakoshi, K., & Rodgers, A. (2020). Kinematic rupture  
681 modeling of ground motion from the M7 Kumamoto, Japan earthquake. *Pure and Applied*  
682 *Geophysics*, 177(5), 2199-2221.  
683

684 Riquelme, S., Medina, M., Bravo, F., Barrientos, S., Campos, J., & Cisternas, A. (2018), W-phase  
685 real-time implementation and network expansion from 2012 to 2017: The experience in Chile.  
686 *Seismological Research Letters*, 89(6), 2237-2248.  
687

688 Ross, Z. E., Meier, M. A., Hauksson, E., & Heaton, T. H. (2018), Generalized seismic phase  
689 detection with deep learning. *Bulletin of the Seismological Society of America*, 108(5A), 2894-  
690 2901.  
691

692 Ruhl, C. J., Melgar, D., Geng, J., Goldberg, D. E., Crowell, B. W., Allen, R. M., ... & Cabral-Cano,  
693 E. (2019), A global database of strong-motion displacement GNSS recordings and an example  
694 application to PGD scaling. *Seismological Research Letters*, 90(1), 271-279.  
695

696 Ruiz, S., & Madariaga, R. (2018). Historical and recent large megathrust earthquakes in Chile.  
697 *Tectonophysics*, 733, 37-56.  
698

699 Rydelek, P., & Horiuchi, S. (2006), Is earthquake rupture deterministic?. *Nature*, 442(7100), E5-  
700 E6.  
701

702 Srivastava, N., Hinton, G., Krizhevsky, A., Sutskever, I., & Salakhutdinov, R. (2014), Dropout: a  
703 simple way to prevent neural networks from overfitting. *The journal of machine learning research*,  
704 15(1), 1929-1958 .  
705

706 Vallée, M., & Douet, V. (2016). A new database of source time functions (STFs) extracted from  
707 the SCARDEC method. *Physics of the Earth and Planetary Interiors*, 257, 149-157.  
708

709 Williamson, A. L., Melgar, D., Crowell, B. W., Arcas, D., Melbourne, T. I., Wei, Y., & Kwong, K.  
710 (2020), Toward near-field tsunami forecasting along the Cascadia subduction zone using rapid  
711 GNSS source models. *Journal of Geophysical Research: Solid Earth*, e2020JB019636.  
712

713 Wu, Y. M., & Zhao, L. (2006), Magnitude estimation using the first three seconds P-wave  
714 amplitude in earthquake early warning. *Geophysical Research Letters*, 33(16).  
715  
716

717 Ye, L., Lay, T., Kanamori, H., & Rivera, L. (2016), Rupture characteristics of major and great ( $M_w \geq$   
718 7.0) megathrust earthquakes from 1990 to 2015: 1. Source parameter scaling relationships.  
719 *Journal of Geophysical Research: Solid Earth*, 121(2), 826-844.

720  
721 Zhu, L., & Rivera, L. A. (2002), A note on the dynamic and static displacements from a point  
722 source in multilayered media. *Geophysical Journal International*, 148(3), 619-627.

723  
724 Zhu, W., & Beroza, G. C. (2019), PhaseNet: a deep-neural-network-based seismic arrival-time  
725 picking method. *Geophysical Journal International*, 216(1), 261-273.

726  
727  
728

729

### 730 **References From the Supporting Information**

731 Duputel, Z., Tsai, V. C., Rivera, L., & Kanamori, H. (2013). Using centroid time-delays to  
732 characterize source durations and identify earthquakes with unique characteristics. *Earth and*  
733 *Planetary Science Letters*, 374, 92-100.

734  
735 Goda, K., Yasuda, T., Mori, N., & Maruyama, T. (2016), New scaling relationships of earthquake  
736 source parameters for stochastic tsunami simulation. *Coastal Engineering Journal*, 58(3),  
737 1650010-1.

738  
739 Graves, R. W., & Pitarka, A. (2010), Broadband ground-motion simulation using a hybrid  
740 approach. *Bulletin of the Seismological Society of America*, 100(5A), 2095-2123.

741  
742 Graves, R., & Pitarka, A. (2015), Refinements to the Graves and Pitarka (2010) broadband  
743 ground-motion simulation method. *Seismological Research Letters*, 86(1), 75-80.

744  
745 LeVeque, R. J., Waagan, K., González, F. I., Rim, D., & Lin, G. (2016), Generating random  
746 earthquake events for probabilistic tsunami hazard assessment. In *Global Tsunami Science: Past*  
747 *and Future, Volume I* (pp. 3671-3692). Birkhäuser, Cham.

748  
749 Mai, P. M., & Beroza, G. C. (2002), A spatial random field model to characterize complexity in  
750 earthquake slip. *Journal of Geophysical Research: Solid Earth*, 107(B11), ESE-10.

751  
752 Melgar, D., LeVeque, R. J., Dreger, D. S., & Allen, R. M. (2016), Kinematic rupture scenarios and  
753 synthetic displacement data: An example application to the Cascadia subduction zone. *Journal*  
754 *of Geophysical Research: Solid Earth*, 121(9), 6658-6674.

755  
756 Melgar, D., & Hayes, G. P. (2017), Systematic observations of the slip pulse properties of large  
757 earthquake ruptures. *Geophysical Research Letters*, 44(19), 9691-9698.

758  
759 Melgar, D., & Hayes, G. P. (2019), The correlation lengths and hypocentral positions of great  
760 earthquakes. *Bulletin of the Seismological Society of America*, 109(6), 2582-2593.

761

762 Mena, B., Mai, P. M., Olsen, K. B., Purvance, M. D., & Brune, J. N. (2010), Hybrid broadband  
763 ground-motion simulation using scattering Green's functions: Application to large-magnitude  
764 events. *Bulletin of the Seismological Society of America*, 100(5A), 2143-2162.  
765  
766 Pasyanos, M. E., Masters, T. G., Laske, G., & Ma, Z. (2014), LITHO1. 0: An updated crust and  
767 lithospheric model of the Earth. *Journal of Geophysical Research: Solid Earth*, 119(3), 2153-2173.  
768  
769 Zhu, L., & Rivera, L. A. (2002), A note on the dynamic and static displacements from a point  
770 source in multilayered media. *Geophysical Journal International*, 148(3), 619-627.  
771  
772



1  
2  
3  
4  
5  
6  
7  
8  
9  
10  
11  
12  
13  
14  
15  
16  
17  
18  
19  
20  
21  
22  
23  
24

# Supporting information for Early warning for great earthquakes from characterization of crustal deformation patterns with deep learning

J-T. Lin<sup>1</sup>, D. Melgar<sup>1</sup>, A. M. Thomas<sup>1</sup>, and J. Searcy<sup>2</sup>

<sup>1</sup>Department of Earth Sciences, University of Oregon, Eugene, Oregon, USA

<sup>2</sup>Research Advanced Computing Services, University of Oregon, Eugene, Oregon, USA

Corresponding author: Jiun-Ting Lin (junting@uoregon.edu)

## Contents of this file

**Text S1, S2**

**Figure S1 to S8**

## Introduction

This supporting information includes details of the rupture scenarios and synthetic waveforms (Text S1), details of the estimated rupture duration (Text S2), and 8 figures supporting the main text.

## Text S1. Details on the rupture scenarios and synthetic waveforms

Underpinning the KL expansion method is the notion that slip on a fault can be modeled as a spatially random field (Mai & Beroza, 2002). Once a correlation function is defined then random draws can be made to obtain a stochastic slip pattern. By comparison to slip inversions from

25 earthquakes worldwide several studies have noted that slip is best modeled by the Von Karman  
 26 correlation function (Mai & Beroza, 2002; Goda et al., 2016; Melgar & Hayes, 2019) where the  
 27 correlation between the  $i$ -th and  $j$ -th subfault in the rupture is defined as

28

$$29 \quad C_{ij}(r_{ij}) = \frac{G_H(r_{ij})}{G_0(r_{ij})} \quad (1)$$

30

$$31 \quad G_H(r_{ij}) = r_{ij}^H K_H(r_{ij}) \quad (2)$$

32

33 where  $K_H$  is the modified Bessel function of the second kind and  $H$  is the Hurst exponent. We set  
 34  $H = 0.4$  based on a recent analysis of large earthquakes between 1990 and 2019 (Melgar &  
 35 Hayes, 2019), which is slightly lower than the value of  $H=0.7$  proposed when stochastic slip  
 36 models were first employed (Mai & Beroza, 2002; Graves & Pitarka, 2010).  $r_{ij}$  is the inter-subfault  
 37 distance given by

38

$$39 \quad r_{ij} = \sqrt{(r_s/a_s)^2 + (r_d/a_d)^2} \quad (3)$$

40 Where  $r_s$  is the along-strike distance and  $r_d$  the along-dip distance. The along-strike and along-  
 41 dip correlation lengths,  $a_s$  and  $a_d$ , control the predominant asperity size in the resulting slip  
 42 pattern (Mai & Beroza, 2002) and scale with indirectly with magnitude as a function of the fault  
 43 length and width according to

44

$$45 \quad a_s = 2.0 + \frac{1}{3}L \quad (4)$$

46

$$47 \quad a_d = 1.0 + \frac{1}{3}W \quad (5)$$

48

49 Once all the parameters of the correlation matrix are defined the covariance matrix is obtained  
50 by

$$51 \quad \widehat{C}_{ij} = \sigma_i C_{ij} \sigma_j \quad (6)$$

52

53 Where  $\sigma$  is the standard deviation of slip which is usually defined as a fraction of mean slip.  
54 Here we set it to 0.9 (LeVeque et al., 2016). Now we can obtain a randomly generated slip pattern  
55 with the statistics as defined above by summing the eigenvectors of the covariance matrix  
56 according to the K-L expansion (LeVeque et al., 2016) such that

57

$$58 \quad s = \mu + \sum_{k=1}^N z_k \sqrt{\lambda_k} v_k \quad (7)$$

59

60 where  $s$  is a column vector containing the values of slip at each of the subfaults for a particular  
61 realization.  $\mu$  is the expected mean slip pattern, we set it to be a vector with enough homogenous  
62 slip over the selected subfaults to match the target magnitude.  $N$  is the maximum number of  
63 summed eigenvectors. We use a reasonably large number of 100 which should give enough  
64 variation of slip complexity (Melgar et al., 2016; LeVeque et al., 2016).  $z_k$  is a scalar randomly  
65 selected from a presumed gaussian distribution with mean 0 and standard deviation of 1.  $\lambda_k$  and  
66  $v_k$  denotes the eigenvalue and eigenvector of the covariance matrix.

67

68 With the stochastic slip pattern in hand, the second step is to define the rupture kinematics.  
69 Here we follow common best practices and a full treatment of this can be found in Graves &  
70 Pitarka (2010, 2015). We set the rupture speed to 0.8 of the local shear wave velocity at the  
71 subfault depth plus some stochastic perturbation to destroy perfectly circular rupture fronts. The  
72 hypocenter is randomly selected from the subfaults that are involved in the rupture to ensure both  
73 unilateral and bilateral ruptures. Rise times are defined to be proportional to the square root of

74 local slip (Mena et al., 2010) but over the entire fault model must on average obey known rise-  
75 time magnitude scaling laws (Melgar & Hayes, 2017). We then use the Dreger slip rate function  
76 to describe the time-evolution at a particular subfault (Mena et al., 2010; Melgar et al., 2016). It is  
77 well-known that the shallow megathrust has slow rupture speeds and long rise times, so for  
78 subfaults shallower than 10km rupture speeds are set to 0.6 of shear wave speed and rise times  
79 are doubled from what is predicted by the scaling by the square root of slip. Below 15km the  
80 previously described rules are used, and between 10 and 15km depth a linear transition between  
81 the two behaviors is employed. This is similar to what is done for continental strike-slip faults  
82 (Graves & Pitarka, 2010). Similarly, the rake vector is set to 90 degrees plus some stochastic  
83 perturbations.

84  
85 Once the slip pattern and its complete time evolution are known, synthetic GNSS waveforms  
86 are generated by summing all the synthetic data from participating subfaults. We use the FK  
87 package, which is a 1D frequency-wavenumber approach (Zhu & Rivera, 2002) and the LITHO1.0  
88 velocity structure (Pasyanos et al., 2014) to generate the Green's functions from all subfaults to  
89 given stations. We focus only on the long period displacement waveforms (<0.5 Hz or 1 second  
90 sampling) since they are less sensitive to small scale crustal structure and are the dominant period  
91 of large earthquakes.

92  
93  
94

## 95 **Text S2. Calculation of estimated rupture duration**

96 We begin the duration estimation by assuming rupture source time function is symmetric (i.e.  
97 rise and decline time are the same). Given the Mw-duration scaling of Duputel et al. (2013),  
98 duration  $T$  can be estimated by

$$99 \quad T = 2.4 \times 10^{-8} \times M_0^{1/3}, \quad (8)$$

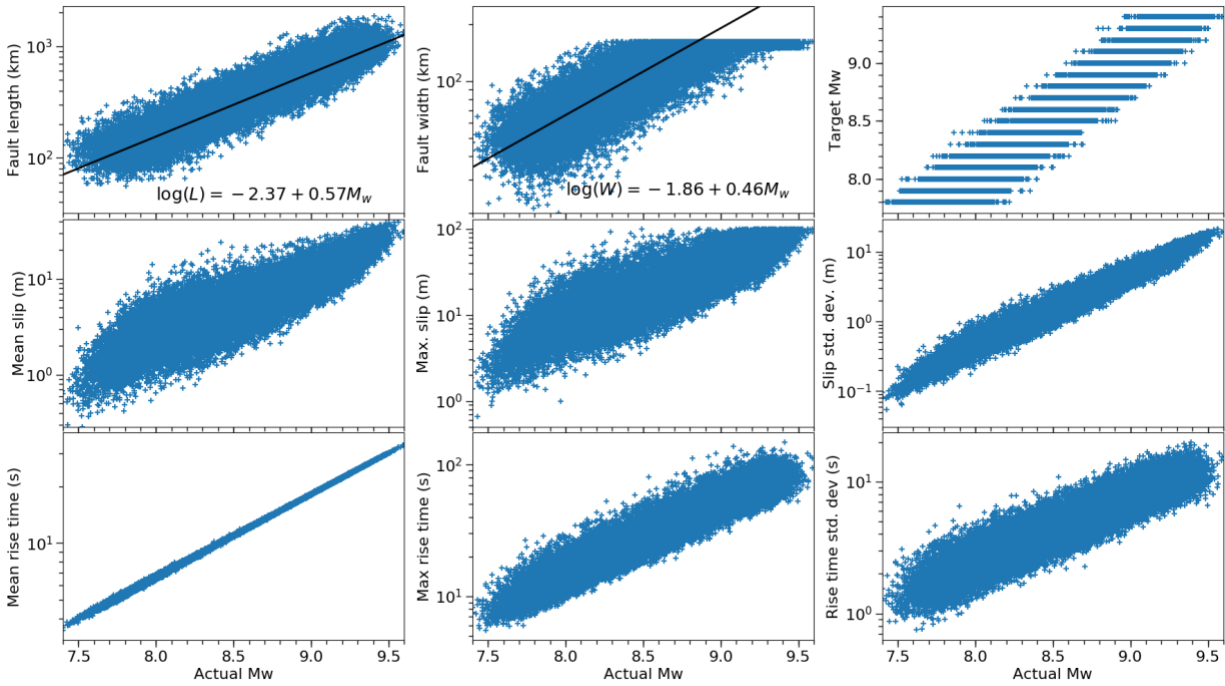
100 
$$M_0 = 10^{(M_w+10.7)\times 1.5}, \tag{9}$$

101 Where the  $M_0$  represents moment in dyne-cm. By plugging the equation (9) into (8) with an  
 102 magnitude  $M_w-0.3$ , we can estimate the duration ratio

103 
$$R = (10^{(M_w-0.3+10.7)\times 1.5} / 10^{(M_w+10.7)\times 1.5})^{1/3} = 71\% \tag{10}$$

104 Thus, the duration of  $M_w-0.3$  can be estimated by 71% of the original  $M_w$  duration.

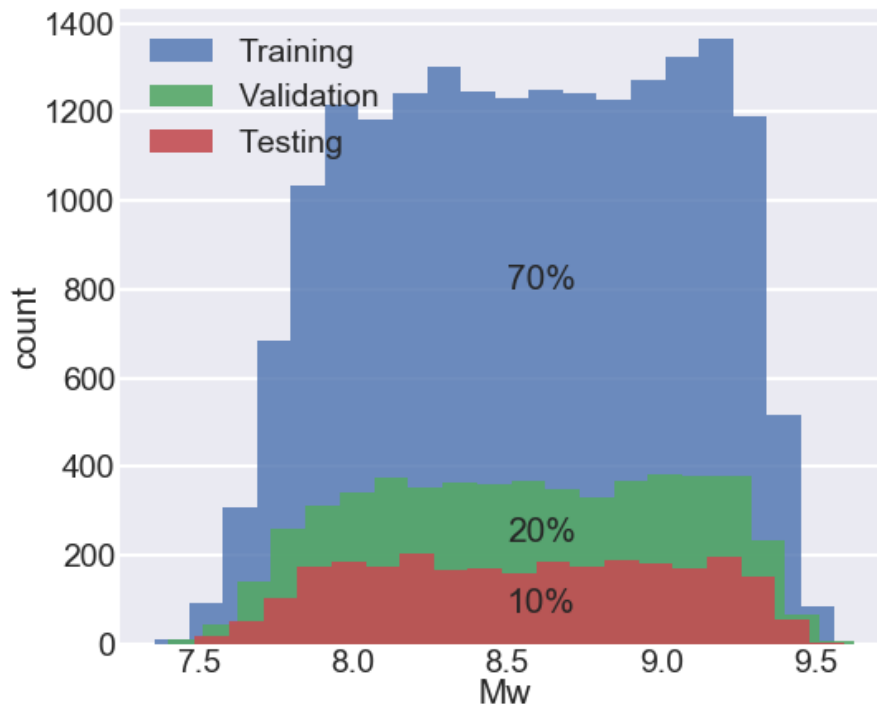
105  
 106  
 107  
 108  
 109  
 110  
 111



112  
 113 **Figure S1.** Source parameters for the 27200 rupture scenarios.

114

115

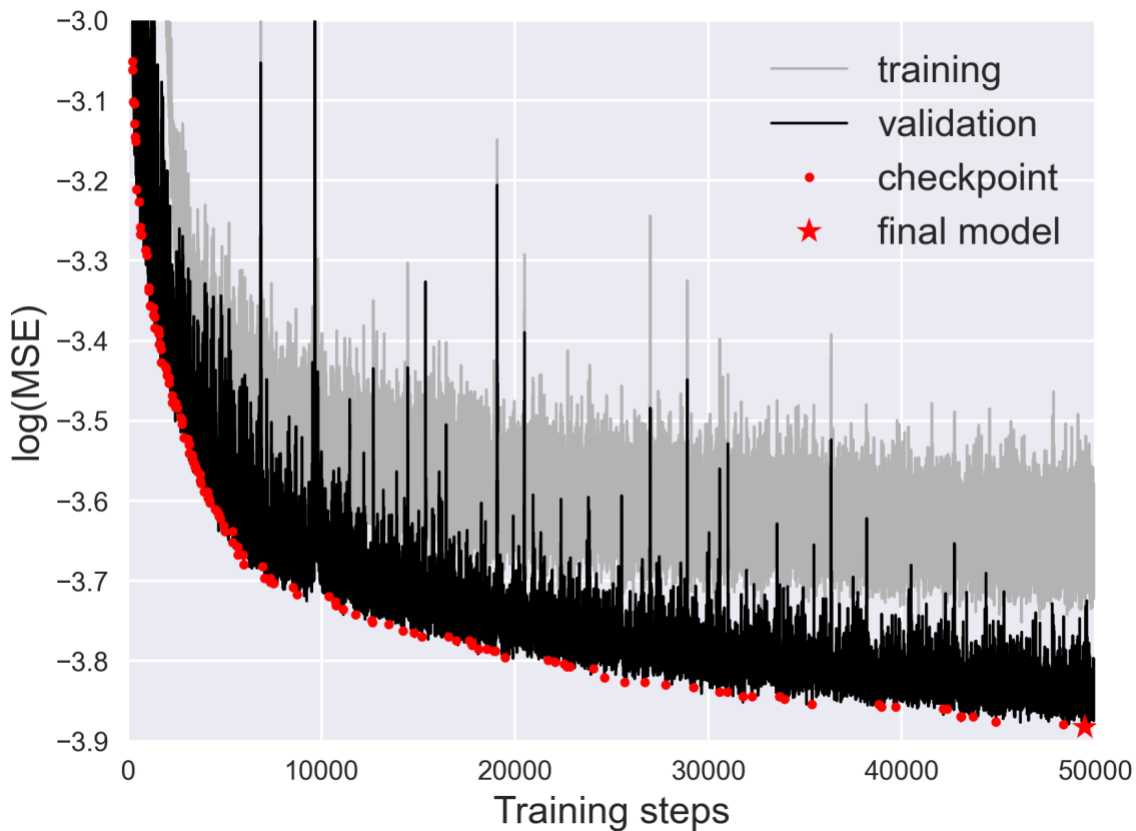


116

117 **Figure S2.** Histogram and partition of training, validation and testing dataset.

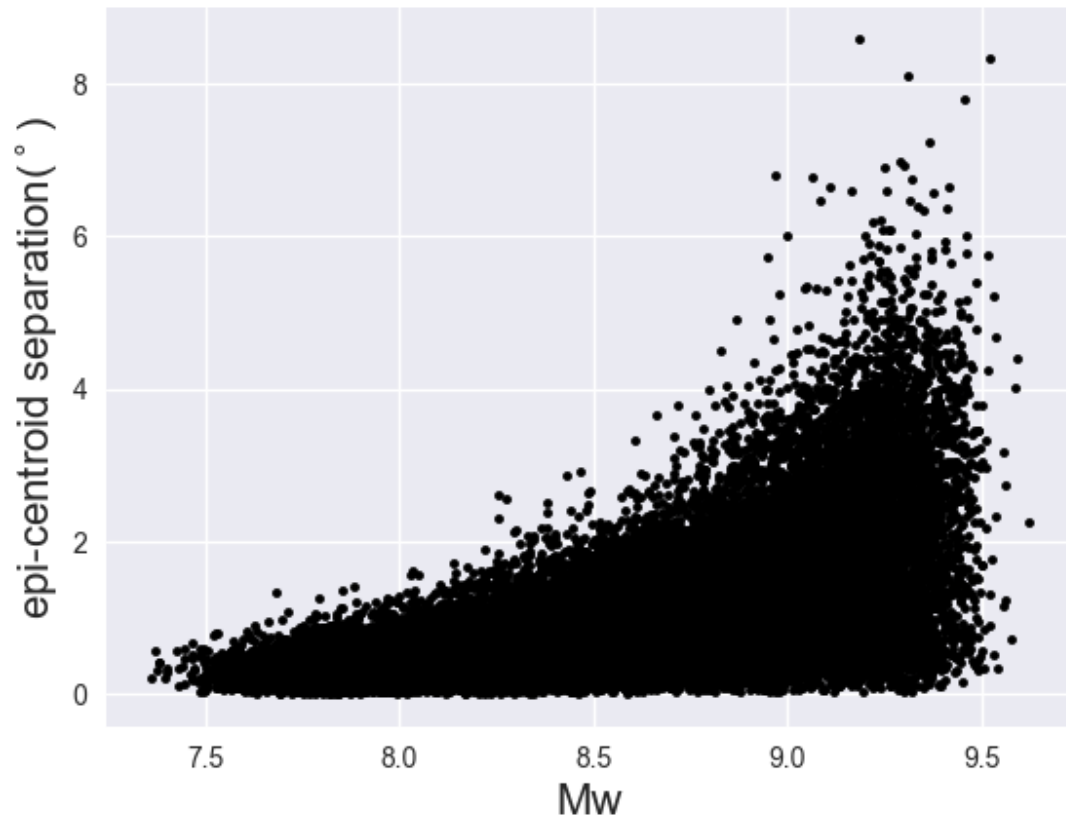
118

119



120

121 **Figure S3.** Training curve for M-LARGE. Light and dark line show the MSE for training and  
 122 validation data, respectively. Red dots denote the checkpoints for the training, with interval of  
 123 every 5 epochs and save the model if the current checkpoint loss is smaller than the previous  
 124 checkpoint loss. Red star represents the final selected model, which has the minimum checkpoint  
 125 loss. Note that the validation loss is smaller than the training loss because dropouts are only  
 126 implemented in the loss calculation.

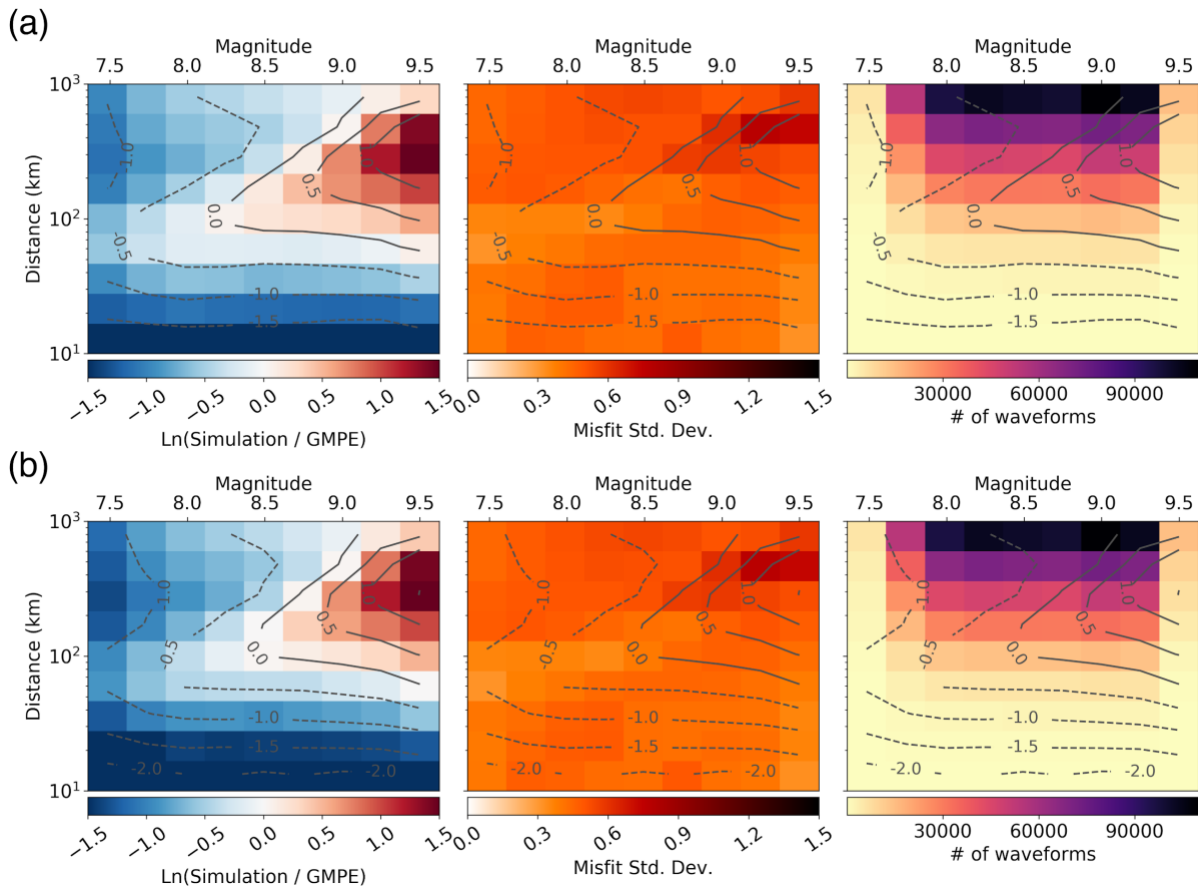


127

128 **Figure S4.** Epicenter and centroid separation for all the 27200 rupture scenarios.

129





130

131 **Figure S5.** Comparison between synthetic data and PGD-Mw scaling of (a) [Melgar et al. \(2015\)](#) and (b)

132 [Ruhl et al. \(2019\)](#). (a) and (b) from left to right shows the misfit of synthetic PGD and PGD-Mw scaling and

133 its contour; standard deviation of the misfit; and distribution of waveforms in count.

134

135

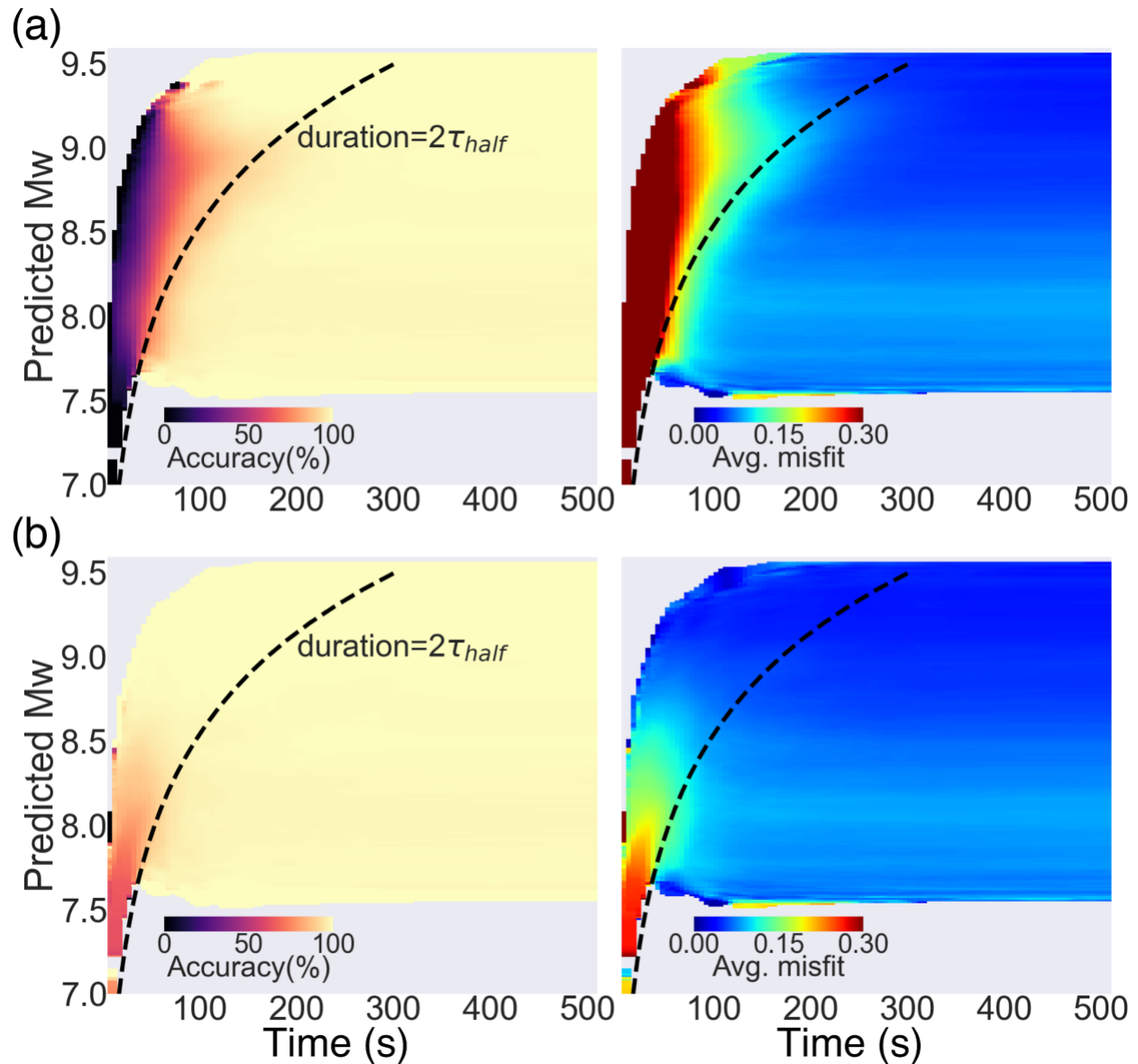
136

137

138

139

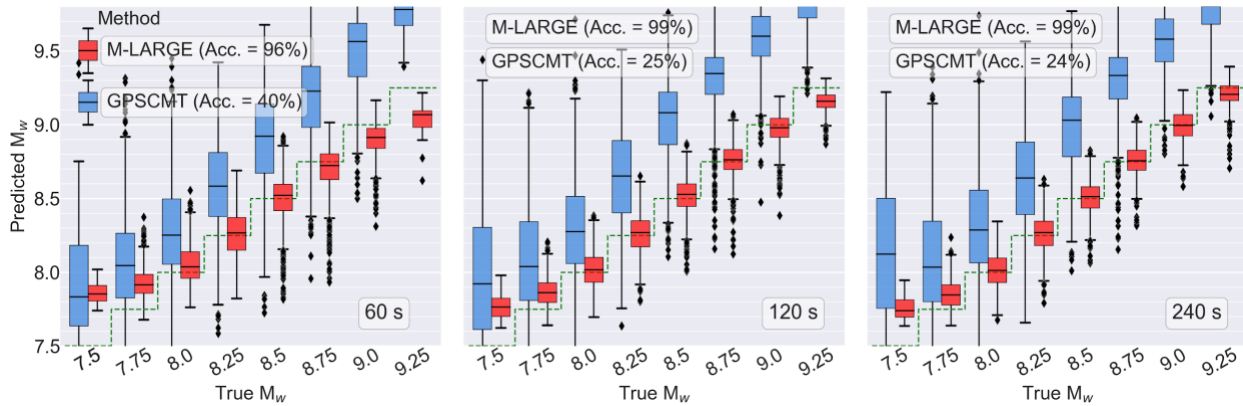
140



141

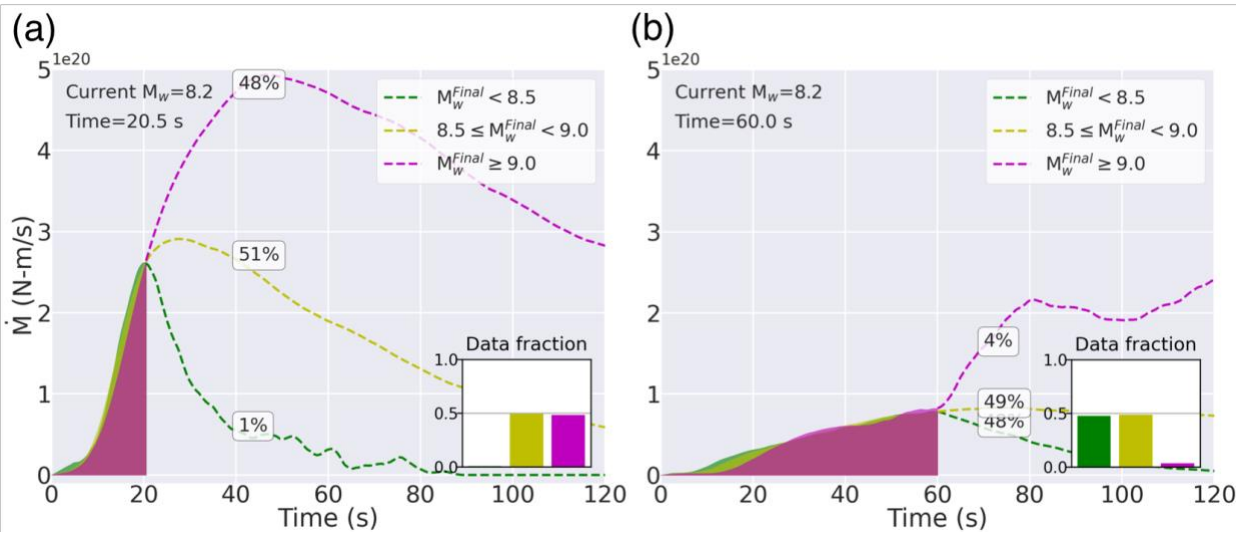
142 **Figure S6.** Model performance for testing dataset. (a) shows the prediction accuracy (i.e. number of  
 143 success prediction/total samples) as a function of time and Mw. Where a success prediction is defined as  
 144 when the predicted and final Mw misfit is <0.3. Dashed line shows the estimated duration. (b) same as (a),  
 145 but define a success prediction is when the predicted and time dependent Mw misfit is <0.3. Note that the  
 146 time dependent Mw is the integration from the STF at current time.

147



148  
 149 **Figure S7.** Similar to the Fig. 2b, but the comparison of the M-LARGE (red) and GPSCMT (blue) predicted  
 150 magnitudes at 60, 120 and 240 s for different magnitude bins. Model accuracies at 60, 120 and 240 s are  
 151 shown in text. The green dashed lines show the 1:1 reference for each magnitude bin.

152



153  
 154 **Figure S8.** Example STFs in our dataset showing the sources are not strongly deterministic but some  
 155 degree of weak determinism. (a) The STFs at 20.5 s have similar shapes and accumulated  $M_w$  of 8.2,  
 156 however, are ambiguous to their final magnitude. The percentage texts denote the fractions of data that  
 157 eventually grow to the designated groups. Dashed lines show the averaged future STFs for each group. (b)  
 158 same as (a) but show the STFs at 60 s. The statistic shows it is less likely (i.e. 4%) that an event can grow  
 159 to a very large event although some large  $M_w$  earthquakes take hundreds of seconds to rupture. The  
 160 possibility is limited according to the current rupture history and the remaining available space of growth  
 161 limited by the subduction zone geometry.

162  
163  
164  
165  
166  
167  
168  
169  
170  
171  
172  
173  
174  
175  
176  
177  
178  
179  
180  
181  
182  
183  
184  
185  
186  
187  
188  
189  
190  
191  
192  
193  
194  
195  
196  
197  
198  
199  
200  
201  
202  
203  
204  
205  
206  
207  
208

## References From the Supporting Information

Duputel, Z., Tsai, V. C., Rivera, L., & Kanamori, H. (2013). Using centroid time-delays to characterize source durations and identify earthquakes with unique characteristics. *Earth and Planetary Science Letters*, 374, 92-100.

Goda, K., Yasuda, T., Mori, N., & Maruyama, T. (2016), New scaling relationships of earthquake source parameters for stochastic tsunami simulation. *Coastal Engineering Journal*, 58(3), 1650010-1.

Graves, R. W., & Pitarka, A. (2010), Broadband ground-motion simulation using a hybrid approach. *Bulletin of the Seismological Society of America*, 100(5A), 2095-2123.

Graves, R., & Pitarka, A. (2015), Refinements to the Graves and Pitarka (2010) broadband ground-motion simulation method. *Seismological Research Letters*, 86(1), 75-80.

LeVeque, R. J., Waagan, K., González, F. I., Rim, D., & Lin, G. (2016), Generating random earthquake events for probabilistic tsunami hazard assessment. In *Global Tsunami Science: Past and Future, Volume I* (pp. 3671-3692). Birkhäuser, Cham.

Mai, P. M., & Beroza, G. C. (2002), A spatial random field model to characterize complexity in earthquake slip. *Journal of Geophysical Research: Solid Earth*, 107(B11), ESE-10.

Melgar, D., LeVeque, R. J., Dreger, D. S., & Allen, R. M. (2016), Kinematic rupture scenarios and synthetic displacement data: An example application to the Cascadia subduction zone. *Journal of Geophysical Research: Solid Earth*, 121(9), 6658-6674.

Melgar, D., & Hayes, G. P. (2017), Systematic observations of the slip pulse properties of large earthquake ruptures. *Geophysical Research Letters*, 44(19), 9691-9698.

Melgar, D., & Hayes, G. P. (2019), The correlation lengths and hypocentral positions of great earthquakes. *Bulletin of the Seismological Society of America*, 109(6), 2582-2593.

Mena, B., Mai, P. M., Olsen, K. B., Purvance, M. D., & Brune, J. N. (2010), Hybrid broadband ground-motion simulation using scattering Green's functions: Application to large-magnitude events. *Bulletin of the Seismological Society of America*, 100(5A), 2143-2162.

Pasyanos, M. E., Masters, T. G., Laske, G., & Ma, Z. (2014), LITHO1. 0: An updated crust and lithospheric model of the Earth. *Journal of Geophysical Research: Solid Earth*, 119(3), 2153-2173.

Zhu, L., & Rivera, L. A. (2002), A note on the dynamic and static displacements from a point source in multilayered media. *Geophysical Journal International*, 148(3), 619-627.